ANL/NSE-22/31

ARDP Natrium Neutronic Methodology

Argonne Neutronic Assessment of ABR-1000

Nuclear Science and Engineering Division

ANL/NSE-22/31

ARDP Natrium Neutronic Methodology

Argonne Neutronic Assessment of ABR-1000

prepared by
Nicolas Stauff, Ting Fei, Mike Smith
Nuclear Science and Engineering Division, Argonne National Laboratory

Prepared for Natrium Demonstration Project – Methods Development
CRADA 2021-21076

May 31, 2022

REVIEW AND APPROVAL

Prepared by:	Nicolas Stauff Nicolas Stauff Primary Author	Date:	5/24/2022
Reviewed by:	Taek K. Kim T.K. Kim Department Manager	Date:	5/31/2022
Approved by:	Tanju Sofu Tanju Sofu Project Manager	Date:	5/31/2022

REVISION HISTORY

Revision No.	Effective Date	Section(s) Affected	Description of Change(s)
0	2022-05-31	All	Initial release.

ABSTRACT

The Natrium Sodium-cooled Fast Reactor (SFR) concept developed by TerraPower, LLC was selected as one of the advanced reactor designs for demonstration under the Advanced Reactor Demonstration Program Natrium Demo project. In collaboration with TerraPower, the Argonne National Laboratory (ANL) team provide independent reviews of the neutronic methodology being used for the Natrium design.

As part of this activity, both the TerraPower and ANL teams agreed to perform independent neutronics analyses of the ABR-1000 reactor problem as a demonstration on the usage of the neutronics methodologies. Comparison of the results from TerraPower and ANL would expose any methodological differences in the modeling approaches.

This report describes and presents the Argonne analysis work on the ABR-1000, and will be provided to TerraPower, along with data files, to complete the comparison study. The comparison will cover the methodology to evaluate the reactivity coefficients for a safety analysis, the shutdown margin, and the reconstructed pin power distribution. The methods and models used to calculate the kinetic parameters and the reactivity coefficients (density, Doppler, axial/radial expansion, etc.) are described in detail with recommendations of specific method options and modelling techniques. The control system reactivity worth and the excess reactivity due to temperature defect are calculated for the shutdown margin analysis. The method to evaluate the excess reactivity is discussed in detail. The pin power reconstruction methodology used in SE2ANL, SE2RCT, and DASSH are discussed in this report. The pin power distribution evaluated by different methods are compared and discussed in the report.

TABLE OF CONTENTS

LIST OF FIGURES

LIST OF TABLES

1 Introduction

Under the Advanced Reactor Demonstration Program Natrium Demo project led by TerraPower, Argonne is providing support to TerraPower with an independent review of the neutronic methodology being used for the Natrium Sodium-cooled Fast Reactor (SFR) design. As part of this activity, both the TerraPower and ANL teams are to independently perform a neutronics analysis of the ABR-1000 reactor problem specified in OECD/NEA UAM-SFR [1]. The ABR-1000 reactor problem was selected because it is a relatively simple and well described benchmark exercise that is sufficiently representative of the Natrium core design work. Comparison of the two results from TerraPower and ANL should expose any methodological differences in the modeling approaches.

This report details the Argonne analysis work on the ABR-1000 and will be provided to TerraPower, along with data files, to complete the comparison study. The ABR-1000 reactor problem does not specify a fuel depletion benchmark, but is focused on follow-on safety analysis given a state point in the ABR-1000 reactor design. Thus the comparison will cover the methodology for generating cross sections, calculating the critical state of the reactor, and generating reactivity coefficients for a safety analysis. For the purposes of the comparison with TerraPower, a shutdown margin evaluation is added along with pin power reconstruction.

The details of the ABR-1000 reactor problem are provided in Section 2. For the ANL contribution, the Argonne Reactor Computation (ARC) suite of neutronic codes is used which is described in Section 3. Some verification analysis work completed with a Monte-Carlo code is also provided for comparison (typical methodology taken at ANL to ensure ARC results are representative). Section 4 covers the methodology for calculating the reactivity feedback coefficients and summarizes the results obtained for ABR-1000. Section 5 covers the methodology for the shutdown margin evaluation and summarizes the results obtained for ABR-1000. Section 6 covers the pin power reconstruction techniques and summarizes the results obtained for ABR-1000. Section 7 summarizes the overall results of this work.

2 ABR-1000 Core Specifications

The ABR-1000 core is a medium-size metallic-fueled SFR concept designed at ANL. It was developed as part of the Global Nuclear Energy Partnership (GNEP) program. The ABR-1000 core modeled in this work is based on the detailed design specifications as described in Reference [1] that was developed under the OECD/NEA sub-group on Uncertainty Analysis in Modeling (UAM) of Sodium-cooled Fast Reactors (SFR-UAM) under the NSC/WPRS/EGUAM.

The ABR-1000 core generates 1,000 MW thermal (i.e. 400 MW electrical). It is a compact design with a conversion ratio of ~0.7 that provides a one-year cycle length with a 90% capacity factor. Conventional (or reasonably proven materials) such as U-Pu-10Zr metallic fuel alloy with HT-9 cladding and HT-9 structural components were used in the ABR-1000 design. The inlet and outlet sodium temperatures are set to be 355°C and 510°C, respectively. Figure 2-1 shows the radial core layout of the ABR-1000 core: it consists of 180 drivers, 114 radial reflectors, 66 radial shields, and 19 control subassemblies.

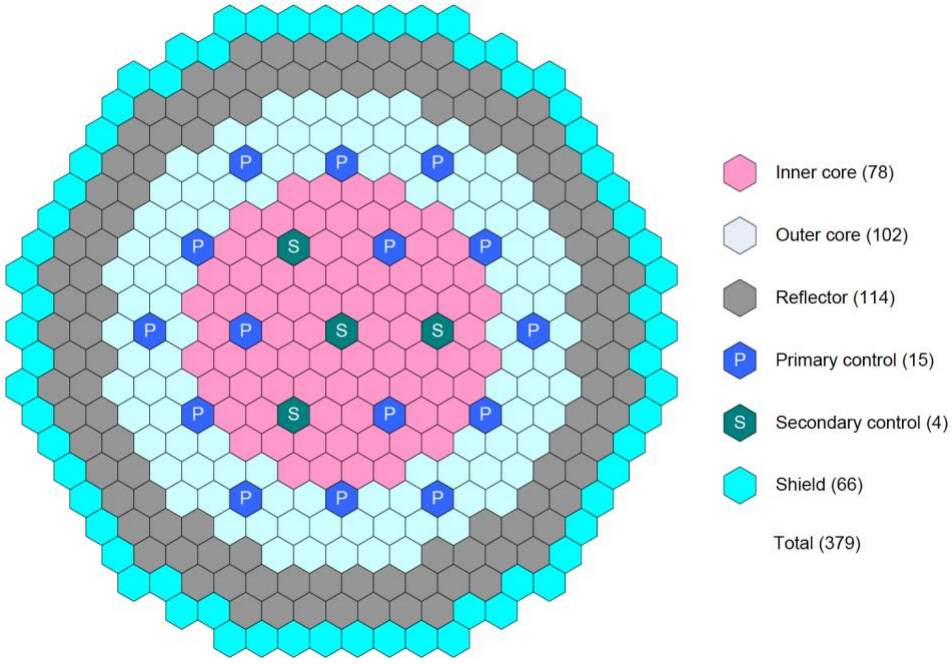

Figure 2-1. Radial layout of ABR-1000 [1].

The flow orifice strategy used to compute the channel-averaged reactivity coefficients are obtained in [2], Figure II.1-9 (right) and shown in Figure 2-2.

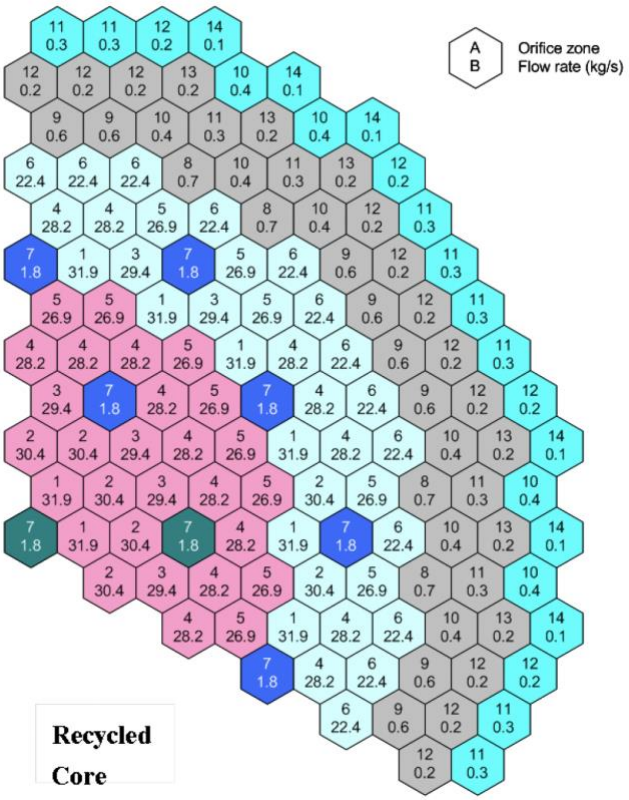

Figure 2-2. Orifice Strategy in Recycled Core of ABR-1000 in [2], Figure II.1-9 (right).

3 Neutronic Methodology Description and Verification

This section provides a detailed description of the methodology used by ANL to build a model of the ABR-1000 reactor problem described in Section 2. The description of the "common" methodology and tools used throughout this report is provided in Section 3.1, while additional specific tools and methodologies are described in Sections 4, 5, and 6. Simple verification of the accuracy of the neutronics simulations used is provided in Section 3.2 through code-to-code comparison of the neutronics results obtained with PyARC [3] to reference Monte Carlo solution (with OpenMC [4]).

3.1 Description of Neutronic Methodology used

The main parts of ARC used for this analysis include MC^2-3 [5], DIF3D [6], GAMSOR [7], PERSENT [8], and DASSH [9]. The inputs, models are both generated and executed with Workbench/PyARC and the VARIANT solver option in DIF3D [10], [11] is used to produce multi-group transport solutions.

3.1.1 XS generation with MC^2-3

The MC^2-3 code is used to obtain 33-group cross-sections for use with DIF3D, GAMSOR, and PERSENT. All of these codes focus on an assembly-homogenized model construction where the fine grained details of the assembly design are replaced with a homogeneous equivalent. The purpose of MC^2-3 is thus to generate region-wise (assembly) cross section data that allows the homogenized model in these codes to provide equivalent results to the original heterogeneous problem being solved. For this work, ANL used the ENDF/B-VII.0 [12] nuclear data library available with MC^2-3 to generate the multi-group cross section library. Depending upon the analysis work being done, several approaches to generating the region-wise cross sections were tested and used. Table 3-1 summarizes the approaches taken for the comparison work.

Table 3-1. MC^2-3 modeling approaches used for different analyses.

Analysis Task	Section	MC^2-3 Step 1	RZ Model	MC^2-3 Step 2
Criticality and Flux (DIF3D)	3.2	1041 gp, hom	TWODANT	33gp, 1D-het
Gamma Heating Calculation (GAMSOR)	4.3	33 gp, 1D-het	n.a.	n.a.
Pin Power Reconstruction (GAMSOR/DASSH)	6	33 gp, 1D-het	n.a.	n.a.
Shutdown Margin (DIF3D)	5	33 gp, hom	TWODANT	33gp
Reactivity coefficients (DIF3D and PERSENT)	4.2.3 & 4.2.6	1041 gp, hom	TWODANT	33gp, 1D-het
	4.2	from Reference		

- **Two-step Methodology Description**

A two-step methodology with a 1D heterogeneous model is used in the base DIF3D calculation to generate the multi-group region-wise cross section data file (ISOTXS). This same approach is not available in the GAMSOR path as the gamma library data cannot presently be processed properly with the two-step methodology. The two-step approach is described, and was verified, in reference [13]. It combines both a full-core region-wise flux condensation step and a 1D-heterogeneous step

in fuel and control rod assemblies, as illustrated in Figure 3-1. The TWODANT [14] code is used for 2-step calculations with a model described in 3.1.1.2. The 1D-heterogeneous models used in furl and control rod regions are described in Section 3.1.1.1.

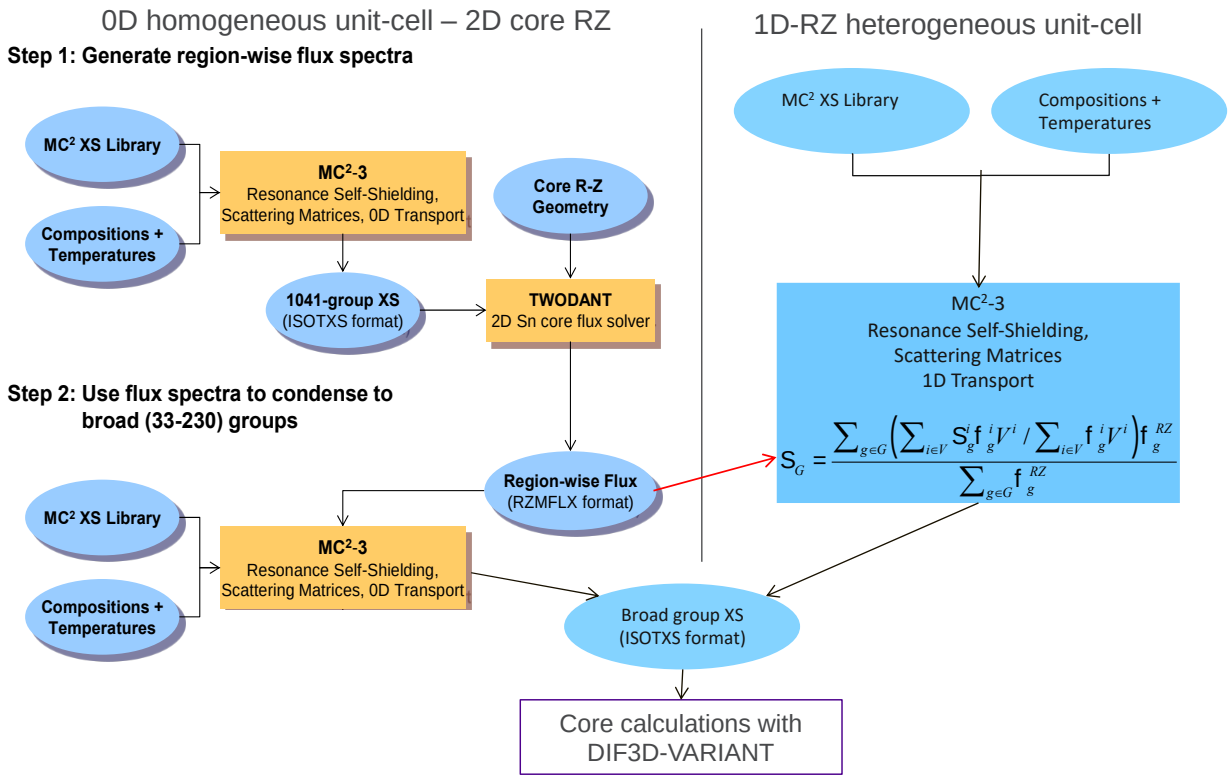

Figure 3-1. Description of 2-step workflow applied for generating multigroup cross-sections with MC²-3.

- **<u>1-step methodology description</u>**

For the GAMSOR/DASSH workflow, a simpler approach is employed to obtain both a neutron and gamma cross-section libraries. This approach is based upon a 1-step scheme using a 1D-heterogeneous treatment (described in Section 3.1.1.1), where the flux spectrum from the fissile region is used as external source to the non-fissile regions.

3.1.1.1 MC²-3 1D heterogeneous models

MC²-3 has a 1D cylindrical or slab lattice flux solver included which is used in this work for fuel and control rod assemblies. This approach allows the analysis methodology to account for spatial self-shielding and the leakage effects of the duct walls. To use the 1D capability, the fuel and control rod assemblies must be cast into an equivalent 1D unit cell geometry. Figure 3-2 provides example unit cell geometries for the control assembly (left picture) and fuel assembly (right picture). In the fuel unit cell, 32 cylindrical regions are required to model the 10 rings of pins, the sodium gap between the duct wall, the duct wall, and the sodium gap between assemblies. As can be seen, only the central fuel pin has the correct representative cylindrical geometry while all of the other cylinders sandwich each consecutive ring of fuel pins between cylinders of cladding

and then cylinders of coolant. The first 30 cylindrical regions define all 10 rings of fuel pins, their cladding, and the surrounding sodium while the last two cylindrical regions are the duct wall and sodium gap between assemblies. The outer radius of the geometry is 8.53 cm and each ring was defined to conserve the volume (and thus mass of each component material) and the solver maximal mesh size was set as 0.2cm. To build the region-wise cross section library, a total of ten 1D models were created, five axial regions of the inner fuel assembly and 5 axial regions of the outer fuel assembly. The equivalent 0D model can be compared against the 1D cylindrical model shown, and MC^2-3 shows ~350 pcm difference in k-infinity

The control rod assembly is converted to 15 cylindrical shells with a total radius of 13.53 cm as seen in the left picture of Figure 3-3. This assembly has only 3 rings of pins and only the central pin retains the physical geometry of a pin. The remaining pins in each ring are sandwiched between cylinders of cladding and coolant leading to 10 total cylindrical rings for the fuel pin lattice and surrounding sodium. The control assembly is double ducted and thus the 11th and 12th ring are the inner duct wall and the sodium gap between the duct walls. The 13th and 14th cylinders are the outer duct wall and sodium gap between adjacent assemblies. The last 5 cm thick ring is filled with a volume homogenized mixture of the uppermost region of the inner fuel assembly. This last ring is removed during the homogenization process but is required to provide a proper neutron source. The heterogeneity effect calculated by MC^2-3 on the K-inf of these unit cells is much larger with around 10% on the primary rods (using natural B4C) and 22% on the secondary rods (using enriched B4C).

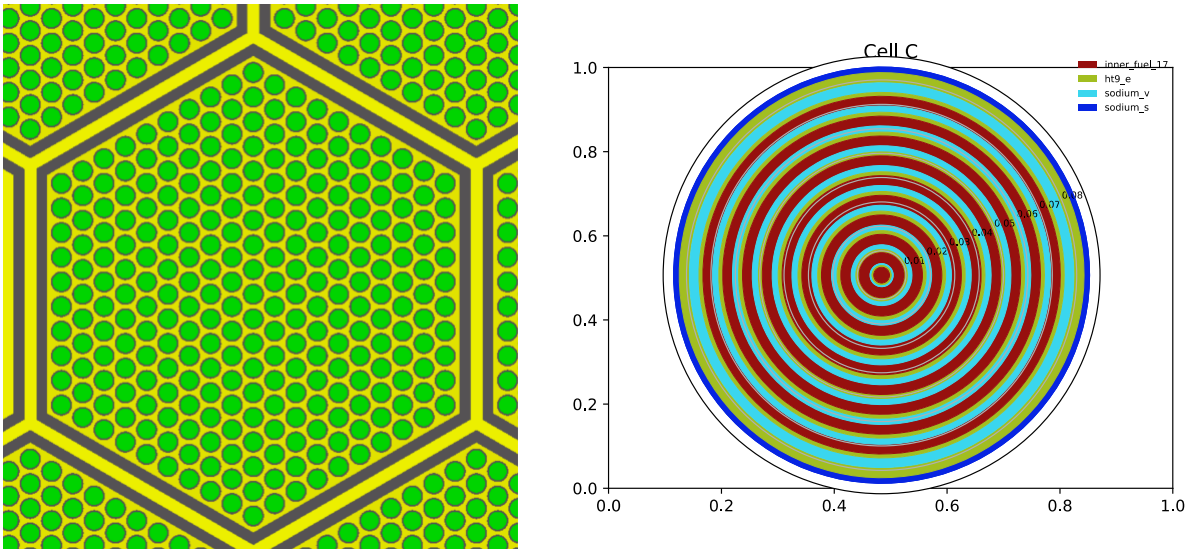

Figure 3-2. Fuel cell (left) and equivalent 1D model (right) used in MC^2-3.

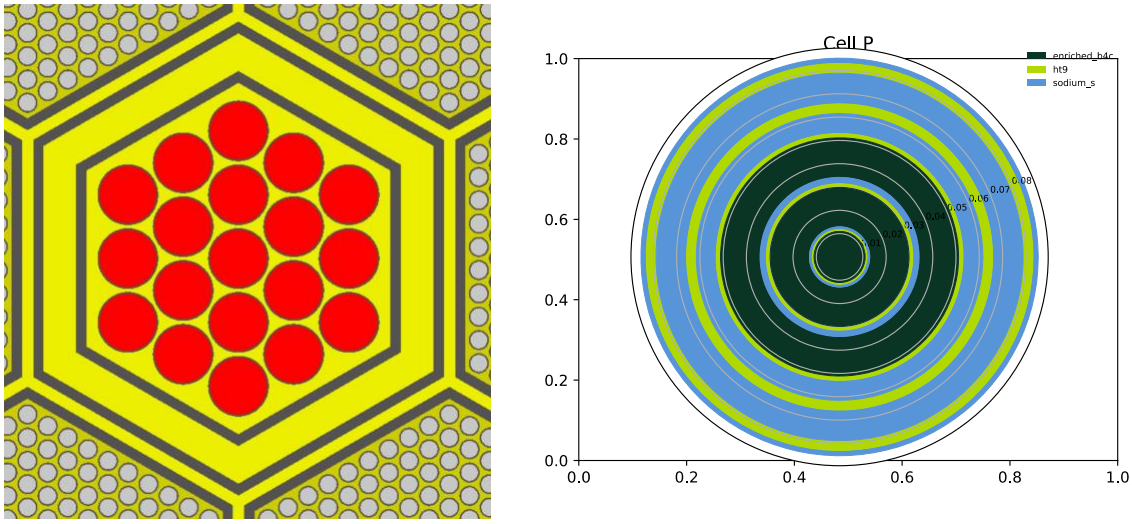

Figure 3-3. Control rod cell (left) equivalent 1D model (right) used in MC^2-3.

3.1.1.2 TWODANT model

A simplified RZ model of the ABR-1000 reactor was built to be representative of the full 3D model. This RZ model is solved by TWODANT with a 1041 energy group structure. The model shown in Figure 3-4 is made of 11 axial regions and 10 radial regions representing the different types of assemblies. The outer radius of the RZ model is 166.1cm and the radius of each cylinder is defined to conserve the volume of the different core regions. The maximum axial and radial mesh size in this model is 10cm, and an S12 angular approximation with a P3 scattering kernel was used.

TWODANT yields a k_{eff} of 1.011 which differs by ~800 pcm with the reference DIF3D-VARIANT results on the 3D hexagonal model (1.019). A perfect agreement between the 2D and 3D model is not required as the MC^2-3 use of the TWODANT solution is only to obtain a better 1041 group flux result in each region that broad group, region-wise cross-section data is to be produced for. This approach typically is most important in core adjacent radial or axial reflector regions where 0D based cross section models yield multi-group cross sections that do not reproduce the criticality or reaction rates observed in the originating heterogeneous system.

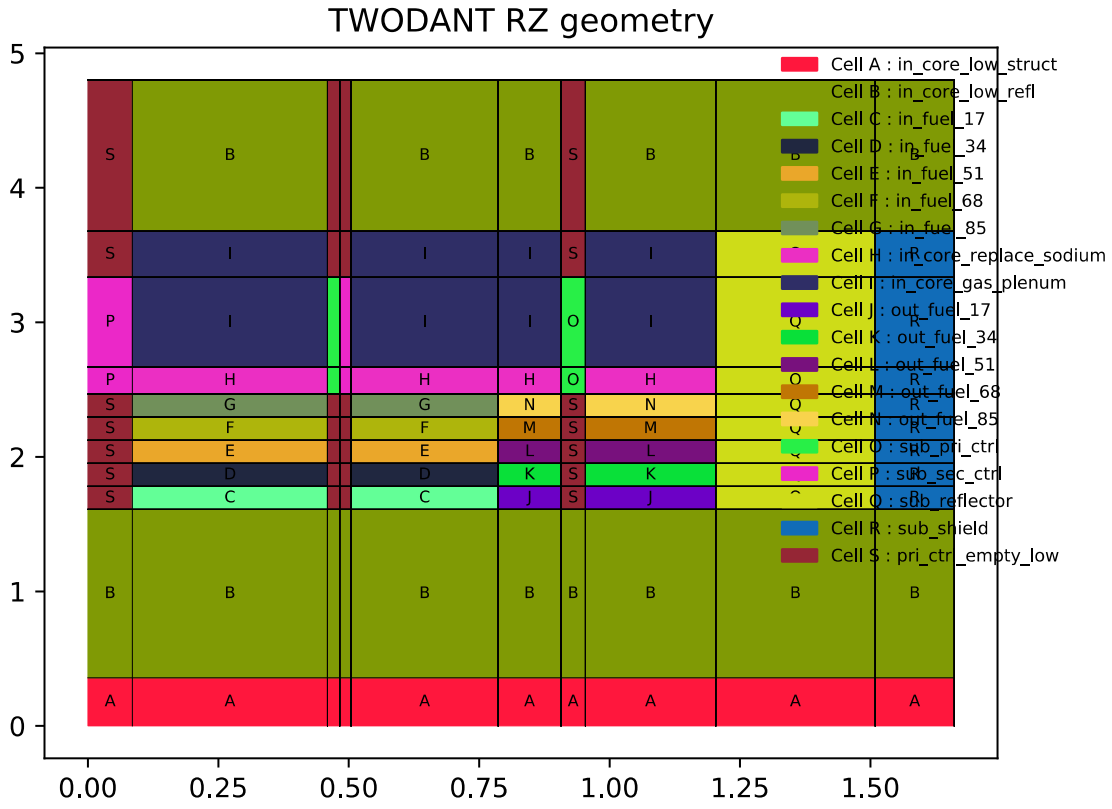

Figure 3-4. Equivalent RZ model used in TWODANT.

3.1.2 Flux calculations with DIF3D/VARIANT

The ABR-1000 reactor has 120 periodic symmetry and thus most of the analysis in this document only requires the modeling of a 120 degree periodic region of the reactor. For the DIF3D and PERSENT calculations in Section 4, a 120 degree periodic model is used. A full core geometry model is used for the shutdown margin calculations in Section 5. The DASSH thermal analysis of the system requires a full core geometry, but the pin power reconstruction results in Section 6 are provided on the 120 degree periodic geometry to reduce the output data to be compared. Because the pin power results originate from the neutronics calculation, it is 120 degree periodic and thus rotationally identical to the full core results.

The DIF3D-VARIANT solver has space-angle settings that the user controls. For the PERSENT and GAMSOR calculations a P_3 angular flux approximation was chosen along with a P_3 anisotropic scattering kernel. A 6^{th} order polynomial approximation of the volumetric source and flux within each mesh was chosen with a first order approximation of the currents used to couple the meshes together. With these settings and the cross-sections processed using the two-step approach, DIF3D yields a k_{eff} of 1.01917.

3.2 Main Results Obtained and Verification

For verification purposes of the reference MC^2-3/DIF3D model developed and used in all the following analyses, an OpenMC model [4] was developed to provide high-fidelity Monte Carlo solution. A fully explicit description of the ABR-1000 is modeled as shown in Figure 3-5. For this analysis, OpenMC uses the ENDF/B-VII.0 nuclear data library. The results obtained are showed in Table 3-2. These results can also be compared against the results from international participants from the OECD/NEA UAM-SFR benchmark, as published in [15].

The k_{eff} obtained with OpenMC is 1.01714+/- 0.00004, which differs from reference MC^2-3/DIF3D by ~200 pcm. This confirms the reference ARC solution compares well with high-fidelity Monte Carlo results. It is striking to see the impact of the cross-section methodology approach on k_{eff}, with 740 pcm of under-estimation when neglecting the heterogeneous treatment, and 455 pcm of under-estimation when neglecting the TWODANT calculation step. For 1-step cross-section treatment, the buckling search option improves k-effective estimate by almost 270pcm.

The reference multigroup cross-section approach using 2-steps with 1D cross-section processing provides also good agreement with Monte Carlo solution on the total control rod worth with less than 4% difference. The 1D heterogeneous processing impacts the Doppler broadening result by ~5%. Otherwise, the cross-section treatment evaluation is observed to have relatively low impact on the sodium void worth calculation, in this particular exercise.

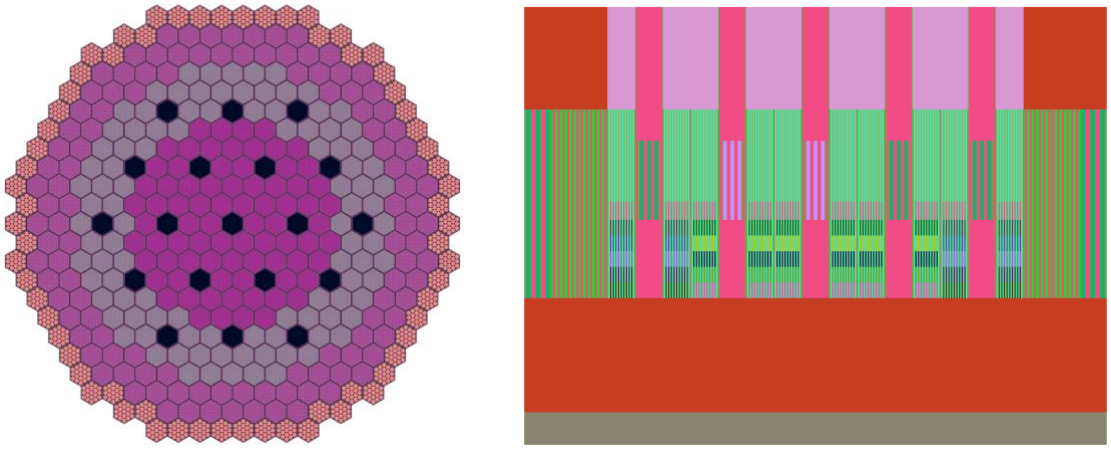

Figure 3-5. Radial (left) and Axial (right) layouts of the ABR-1000 model used in OpenMC.

Table 3-2. Impact of different cross-section processing methods on ABR-1000 results.

MC^2-3 options	n/a	1 Step - Hom – w/o BS	1 Step - Hom with BS	1 Step – 1D het	2 Steps - Hom	2 Steps – 1D het
Flux solver	OpenMC	DIF3D	DIF3D	DIF3D	DIF3D	DIF3D
k_{eff}	1.01714+/- 0.00004	1.00417	1.00691	1.01415	1.01155	**1.01917**
Primary and secondary rod worth [pcm]	9,792 +/- 6	11,165	11,109	9,860	11,247	**10,100**
Sodium void worth [pcm]	1,521 +/- 6	1,535	1,660	1,466	1,598	**1,595**
Doppler Constant [pcm]	-372 +/- 8	-386	-375	-412	-375	**-393**

4 Reactivity Coefficients and Kinetics Parameters

This section details the methodology used to obtain reactivity coefficients appropriate for the SAS4A point kinetics model of the ABR-1000 reactor described in Section 2. Reactivity coefficients and kinetics parameters are typically obtained at ANL for use in the safety analysis of a sodium-cooled fast reactor with SAS4A/SASSYS-1. They can also be used in other design analyses such as shutdown margins (as discussed in Section 5) or as part of the predictive analysis comparison work against experimental measurements. For transient analysis, the reactivity coefficients of interest include:

a. Sodium, structure and fuel density coefficients
b. Thermal induced Doppler effects for the fuel in a voided and flooded states
c. Radial expansion coefficient due to thermal expansion
d. Thermal expansion of the control rod driveline (upper mounted control rods only)

Because most of the SAS4A analysis work uses a point kinetics based model, the kinetics parameters include the delayed neutron fraction and prompt neutron lifetime. The sodium void worth and axial expansion coefficient are also obtained in this work for comparison purposes although they are not used in a conventional SAS4A transient model. In addition to these aspects, the gamma and neutron power distribution is part of the SAS4A input. Results are provided in this section together with the attached detailed excel spreadsheet "ABR1000_ReactivityCoeff_ANL.xls".

4.1 Methodology Description

PERSENT is a perturbation theory and sensitivity theory analysis software based upon the DIF3D-VARIANT solver. The perturbation theory feature was built primarily for use in generating spatial distributions of a reactivity coefficient as is desired for SAS4A. In this regard, all of the reactivity coefficients described above can be assessed with PERSENT although in some cases (radial expansion and control rod driveline) it is more practical to just use DIF3D given the desired output. The mesh-wise contribution to the reactivity coefficient can be exported from PERSENT in table form or in a data file that can be visualized with software such as VISIT.

For comparison purposes with TerraPower, only the total worth of a given perturbation and sums over specific axial regions for a given set of SAS4A "channels" (described as orifice zones in Section 2) are provided in this report. Every reactivity coefficient is obtained by starting with the nominal or base state of the reactor and defining a perturbed state. The reactivity coefficient is calculated as the change in the reactivity scaled by the change required to cause the perturbed state (typically a temperature induced perturbation will yield worth/C). Table 4-1 lists how the perturbed states are defined relative to the base state for each reactivity coefficient. For the kinetics parameters, the base state forward and adjoint flux solution is combined with the delay cross section data. The coefficients where PERSENT is not used are denoted in the Code column of the table with DIF3D. These calculations are equivalent to the exact perturbation methodology of PERSENT and are done this way due to historic limitations of perturbation theory codes on geometric perturbations. With recent changes to PERSENT, all of the reactivity coefficients listed can be obtained using the exact perturbation theory option, but the output is not really usable in the context of SAS4A and is not done for this analysis effort.

Table 4-1. Method used for reactivity coefficients calculation (greyed boxes are not used for SAS4A analyses).

	Perturbed State Change of Base State	Code	Method calculation	XS updated
Sodium density coefficient	all sodium density multiplied by 0.99	PERSENT	1st order perturbation	No
Fuel density coefficient	fuel density multiplied by 0.99 (including Zr and FP) traces of fuel added to upper region			
Structure density coefficient	All HT9 and B4C structure density multiplied by 0.99			
Doppler coefficient (flooded or voided)	Doubling of fuel temperature in reference or voided configurations			Yes
Sodium void worth	Flowing sodium density in driver fuel assemblies, in & above fuel regions, multiplied by 1e-10		Exact perturbation	Yes
Axial expansion coefficient	1% increase in driver fuel height, reduced fuel/structure densities	DIF3D	Exact perturbation	No
Radial expansion coefficient	1% increase in assembly pitch, reduced densities from solid material			
Control rod driveline	5cm rod insertion			

From Table 4-1, two types of perturbation options for PERSENT are used:

- First order perturbation theory (FOP): for small perturbations, the flux solution does not change significantly (i.e. 5th significant digit changes or less in the mesh-wise multi-group flux solution). In these cases, the reactivity coefficients are proportional to the flux weighted integral of the material (or cross section) changes between the base and perturbed state. The first order perturbation is typically referred to being in the linear regime of the perturbation response. To compute the worth, PERSENT takes whatever perturbation is provided by the user and scales it to the linear regime (where the flux solution is known to not be impacted by the perturbation), computes the reactivity worth, and then scales the result back to the magnitude consistent with the user provided perturbed state. The base state forward and adjoint flux solution is needed to compute all first order perturbation coefficients.
- Exact perturbation theory (EP): for some reactivity coefficients in the SAS4A point kinetics model, the reactivity coefficient is not broken into mesh wise contributions but handled with core-wide factors. For perturbations involving geometric changes, perturbation theory codes could not historically provide first order perturbation results and thus exact perturbation would be used. For the listed set of coefficients SAS4A desires the first order perturbation result which can be obtained using exact perturbation theory if the perturbation is small. The intention of the magnitude of the perturbation described in Table

4-1 for the exact perturbation cases (sodium void worth excluded) has been determined to reliably be consistent with the desired first order perturbation result. In PERSENT, the base state adjoint flux and perturbed state forward flux solutions are required to provide a spatial distribution of the reactivity worth.

As can be seen from Table 4-1, the reactivity coefficients selectively rely upon re-evaluation of the multigroup cross-sections. In these cases, the MC^2-3/TWODANT workflow described in Section 3.1.1 is executed on the perturbed state described in the table to produce cross sections for that perturbed state. In practice, all of the isotopic cross sections in the homogenized regions of the perturbed state are altered when this is done.

As stated earlier, the desired reactivity coefficients is worth/K or worth/kg. To do this, thermal expansion coefficients for the various materials are needed to convert the assumed geometry change, typically 1%, into a temperature perturbation. The thermal expansion coefficients used by ANL are taken from reference [1] and are displayed in Table 4-2.

Table 4-2. Linear thermal expansion coefficients assumed for this study [1].

	Sodium	HT9	UPuZr	SS316
T (°C)	432.5	432.5	534	355
α (1/T)	9.48E-05	1.39E-05	1.76E-05	1.75E-05
ΔT(°C / %perturbed)	35.40	726.69	573.92	576.21

4.2 Reactivity Coefficients Calculations

The global reactivity coefficients computed in this study for the ABR-1000 are displayed in Table 4-3. The following sections provides a detailed description of the methodology and assumptions used to compute these different reactivity coefficients and kinetics parameters.

Table 4-3. Global results for the reactivity coefficients.

Coefficient	**Unit**	**Value**
k_{eff} (unperturbed)		1.01917
Axial expansion	[pcm/K]	-0.19
Radial expansion	[pcm/K]	-1.05
Fuel density	[pcm/K]	-0.691
Structure density	[pcm/K]	0.0360
Sodium density	[pcm/K]	0.425
Doppler (flooded) Constant	[pcm]	-393
Sodium void worth	[$]	4.84
Doppler (voided) Constant	[pcm]	-265
Control Rod Driveline	[pcm/cm]	-48.1

Beta-Effective	[pcm]	330

4.2.1 Kinetics parameters

Kinetics parameters are computed with PERSENT using the base state forward and adjoint flux solutions and the delay cross section data (DLAYXS) generated with MC^2-3. The weighting with the forward and adjoint is done consistent with the point kinetics formulation being used in SAS4A as is the case for all of the reactivity coefficients. The coalesced kinetics parameters [8] are provided in Table 4-4 where the total delayed neutron fraction is 330 pcm, and the prompt neutron lifetime is 0.421 μs.

Each fissioning isotope (e.g. U-235, U-238, Pu-239) in a reactor yields a different set of product isotopes, those which emit neutrons are called precursor isotopes. Each precursor isotope has its own decay rate and the conventional point kinetics scheme lumps the isotopes together into a "family" which ideally have similar decay rates. The coalescing process is the means of weighting the decay behavior across fissioning isotopes to yield an effective set of data which models the collective behavior of all fissioning isotopes. The coalesced β and λ results for each family are provided in the table for completeness of the data actually provided to SAS4A. U-238 is the main contributor to delayed neutron population accounting for 44% of the β_{eff}, while Pu-239 contributes to 34%, and the rest coming from Pu-240 (7%) and Pu-241 (10%).

Table 4-4. Kinetics parameters.

β_{eff}	3.30E-03	
Λ_g (s)	4.13E-07	
Λ_p (s)	4.21E-07	
Family	β_{family}	λ_{family}
1	7.71E-05	1.34E-02
2	6.07E-04	3.08E-02
3	4.87E-04	1.18E-01
4	1.18E-03	3.09E-01
5	6.89E-04	8.83E-01
6	2.54E-04	2.95E+00

4.2.2 Sodium density coefficient

The density of all sodium everywhere in the core (flowing and stagnant in driver fuel, reflector, shielding, control/safety rod, etc.) is multiplied by 0.99. The density of all other materials remains unchanged. The coolant density feedback coefficients were calculated using first order perturbation theory without updating the multi-group cross-sections. The resulting reactivity feedback coefficient required for SAS4A safety analysis is a change in reactivity per unit mass of sodium in (Δk/k-kg) which PERSENT will export given it computes the isotopic mass change in the base and perturbed states.

The total sodium density coefficient is +15.1 pcm/%, which translates into +0.425 pcm/K assuming the sodium thermal expansion coefficient in Table 4-2. The 3D distribution of the sodium density coefficient expressed in (Δk/k-kg) is shown in Figure 4-1. The results shown have the sign

flipped from the expected results as the base to perturbed state mass change was negative (1.0 to 0.99 density change) leading to a negative worth/kg result. When the thermal expansion coefficient is used, the sign flips accordingly. Ignoring this detail, the reduction in sodium density internal to the core is correctly positive (shown as negative) while reduction in the upper plenum is correctly negative (shown as positive) due to the increased core leakage. This information is also compiled for each axial region within each orifice zone in Table 4-5.

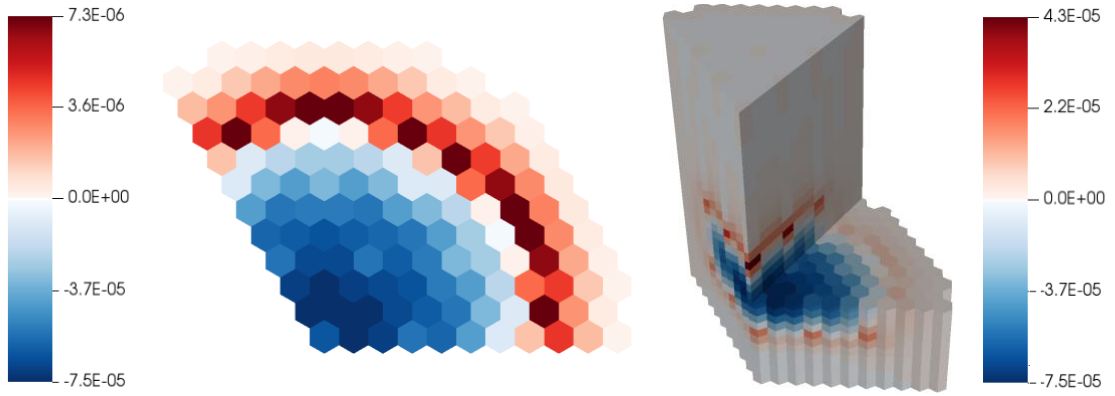

Figure 4-1. Distribution of sodium density coefficient (Δk/k-kg) throughout the core (right) and on a radial slice at z=200cm (left).

Table 4-5. Sodium density coefficients (Δk/k-kg) in each orifice zone.

Fuel Assembly Orifice Zone						
Height (m)	**1**	**2**	**3**	**4**	**5**	**6**
0.3576	-4.60E-12	-6.35E-12	-5.70E-12	-3.86E-12	-3.20E-12	-8.04E-13
1.6092	6.57E-07	4.77E-07	5.10E-07	6.41E-07	6.36E-07	5.44E-07
1.7808	-9.44E-06	-1.28E-05	-1.18E-05	-7.88E-06	-5.92E-06	4.54E-06
1.9524	-3.98E-05	-4.76E-05	-4.46E-05	-3.48E-05	-2.91E-05	2.26E-06
2.124	-4.94E-05	-5.82E-05	-5.48E-05	-4.33E-05	-3.66E-05	1.37E-06
2.2956	-3.38E-05	-3.99E-05	-3.75E-05	-2.97E-05	-2.50E-05	2.28E-06
2.4674	-1.74E-06	-3.16E-06	-2.78E-06	-1.49E-06	-7.08E-07	4.33E-06
2.668	1.04E-05	1.10E-05	1.08E-05	9.10E-06	8.41E-06	4.09E-06
3.6781	7.65E-07	8.51E-07	8.30E-07	6.59E-07	6.41E-07	3.17E-07
4.802	-3.20E-10	-4.15E-10	-3.86E-10	-2.78E-10	-2.28E-10	-2.82E-11

Control Rod Orifice Zone		**Shielding and Reflectors Orifice Zone**							
Height	**7**	**Height**	**8**	**9**	**10**	**11**	**12**	**13**	**14**
0.3576	-4.24E-12	**0.3576**	-4.35E-13	-1.32E-13	1.26E-13	3.76E-13	2.86E-13	2.52E-13	2.60E-13
1.6092	8.44E-07	**1.6092**	3.14E-07	2.53E-07	1.21E-07	7.05E-08	8.06E-08	6.02E-08	2.08E-08
2.4674	-7.86E-06	**3.6781**	2.55E-06	2.37E-06	9.51E-07	3.76E-07	6.39E-07	5.24E-07	3.29E-08
3.335	1.17E-06	**4.802**	-2.22E-11	-2.45E-12	-3.11E-14	2.43E-12	3.12E-12	2.49E-12	1.49E-12

4.802	-1.57E-09

For the sodium density coefficient, a sensitivity analysis was carried out to show the impact of the perturbation calculation methodology used in PERSENT and the results are compiled in Table 4-6. From the results shown, the first order perturbation approach can be confirmed to provide a reactivity coefficient consistent with the linear regime of the perturbation for all provided inputs. The exact perturbation theory results show a clear dependence on the magnitude of the perturbation but given a small enough perturbation, the first order perturbation result is reproduced. Larger perturbation (0.001) clearly show non-linear effects where the EP provides different results when compared with FOP results.

The last set of results in Table 4-6 demonstrate the impact of re-evaluating the multi-group cross sections for each perturbed state. These results do not display a monotonic convergence as the perturbation becomes increasingly small and none of the results are consistent with those when the cross sections are not re-evaluated. This behavior is not too surprising as the core-wide interaction of the perturbation and flux levels is quite complex. The non-linear effect observed on large perturbations (0.001) becomes even more significant when considering update of the perturbed cross-sections.

To determine which approach should be used, one must understand that point kinetics is an engineering equation that requires past experience on modeling a given reactor system. In that regard, the modeling methodology based upon the first order perturbation reactivity coefficients was demonstrated to provide the most accurate representation of the reactor for several experiment measurements. It is noted that the first order perturbation result will yield the largest reactivity worth response for this reactivity coefficient.

Table 4-6. Global Sodium Density Coefficient Results for Different Perturbations

PERSENT methodology	Density Factor	Worth pcm/kg
First order perturbation where cross sections are not updated	0.999	-0.138
	0.99	-0.137
	0.9	-0.137
	0.75	-0.137
	0.001	-0.137
Exact perturbation where cross sections are not updated	0.999	-0.138
	0.99	-0.137
	0.9	-0.136
	0.75	-0.133
	0.001	-0.103
Exact perturbation where cross sections are updated	0.999	-0.126
	0.99	-0.128
	0.9	-0.125
	0.75	-0.120
	0.001	-0.054

4.2.3 Sodium void worth

The sodium void worth calculation considers voiding of flowing sodium (sodium density is multiplied by 10^{-10}) in the fuel assemblies, in and above the driver fuel region. The flowing sodium only considers sodium outside the fuel pin cladding and within the duct of the fuel assemblies. The density of all other materials remains unchanged. The sodium void worth coefficients were calculated using exact perturbation theory while updating the multi-group cross-sections. For the cross section generation in MC^2-3, the voided sodium concentration in the lattice calculations (Figure 3-2) calculation is capped at 10^{-4} at/cm-barn (reference density multiplied by 0.005) to avoid divergence of the built in flux solver.

It should be noted that SAS4A/SASSYS-1 code will not directly use the sodium void worth coefficient, which is only calculated as an informative neutronic metric of the reactor design and to support the calculation of the voided Doppler coefficient (described in Section 4.2.6). The total sodium void worth is 1,595 pcm or \$4.84 using the base state β. The distribution of the sodium void worth is shown in Figure 4-2 in (Δk/k-kg). Because the perturbation is similar, the void worth distribution is similar to that observed earlier in the sodium density reactivity coefficient. This information is compiled in (Δk/k) for each axial region within each orifice zone in Table 4-7.

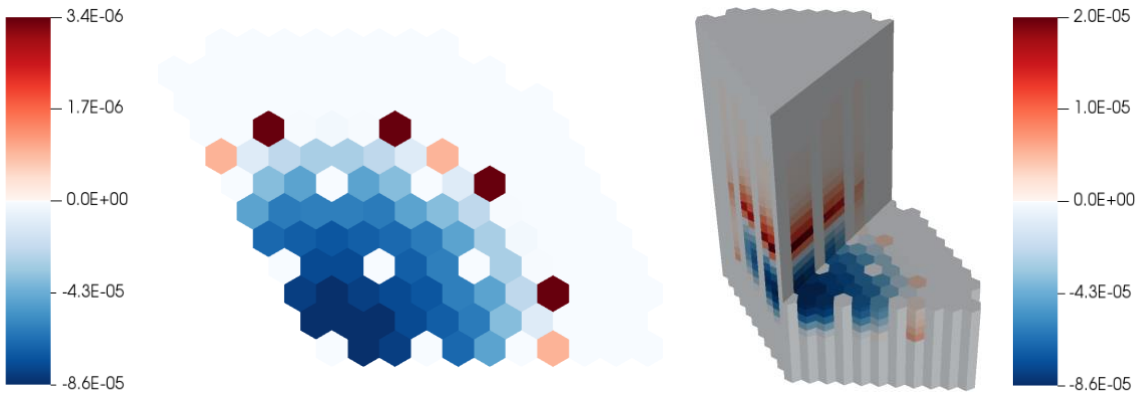

Figure 4-2. Distribution of sodium void worth (Δk/k-kg) throughout the core (right) and on a radial slice at z=200cm (left).

Table 4-7. Sodium void worth (Δk/k) in each orifice zone.

Fuel Assembly Orifice Zone						
Height (m)	**1**	**2**	**3**	**4**	**5**	**6**
0.3576	-8.83E-12	-7.49E-12	-6.97E-12	-1.37E-11	-9.99E-12	-5.62E-12
1.6092	-4.96E-06	-3.78E-06	-3.74E-06	-8.65E-06	-6.96E-06	-3.96E-06
1.7808	2.93E-04	3.00E-04	2.77E-04	4.64E-04	3.06E-04	-1.74E-04
1.9524	1.10E-03	9.96E-04	9.33E-04	1.80E-03	1.30E-03	-6.88E-05
2.124	1.34E-03	1.20E-03	1.13E-03	2.20E-03	1.61E-03	-2.84E-05
2.2956	9.01E-04	8.10E-04	7.61E-04	1.49E-03	1.08E-03	-7.28E-05
2.4674	3.18E-05	5.51E-05	4.83E-05	5.41E-05	1.67E-05	-1.66E-04
2.668	-3.67E-04	-2.97E-04	-2.88E-04	-6.07E-04	-4.86E-04	-2.14E-04
3.6781	-2.13E-04	-1.79E-04	-1.74E-04	-3.47E-04	-2.92E-04	-1.37E-04
4.802	2.18E-07	2.14E-07	1.98E-07	3.59E-07	2.52E-07	2.00E-08

Control Rod Orifice Zone		Shielding and Reflectors Orifice Zone							
Height	**7**	**Height**	**8**	**9**	**10**	**11**	**12**	**13**	**14**
0.3576	-6.67E-12	**0.3576**	-1.72E-12	-2.62E-12	-1.60E-12	0.00E+00	0.00E+00	0.00E+00	0.00E+00
1.6092	-4.41E-06	**1.6092**	-8.31E-07	-1.30E-06	-8.07E-07	-5.09E-07	-6.74E-07	-2.13E-07	-5.60E-08
2.4674	4.78E-05	**3.6781**	-5.83E-05	-1.03E-04	-5.76E-05	-2.57E-05	-5.81E-05	-2.10E-05	2.20E-08
3.335	-1.01E-04	**4.802**	-1.33E-10	-3.52E-10	-2.43E-10	-8.05E-11	-9.65E-11	-2.80E-11	-1.10E-11
4.802	1.34E-07								

4.2.4 Fuel density coefficient

The fuel density reactivity coefficient is defined by multiplying the fuel isotope atom densities, including zirconium and fission products, by a factor of 0.99. For this coefficient, traces of the uppermost axial fuel composition are added to the regions directly above the fuel (the displaced bond sodium in ABR-1000) to provide an estimate of the fuel density reactivity coefficient in this region. This modification is done by replacing 0.01% of the sodium volume with the fuel composition. The geometry and density of all other components are unchanged. The fuel density reactivity coefficient was calculated with the first order perturbation theory option in PERSENT without updating the multi-group cross-sections.

The resulting reactivity coefficient is a change in reactivity per unit mass of fuel expressed in (Δk/k-kg). The total fuel density coefficient is -397 pcm/% perturbed fuel density, which becomes -0.69 pcm/K using the linear expansion coefficient of UPuZr. The 3D distribution of the fuel density coefficient is shown in Figure 4-3 and the axial distribution in all orifice zones are shown in Table 4-8. Only fuel assembly channels are shown since the reactivity coefficient is zero in non-fuel regions.

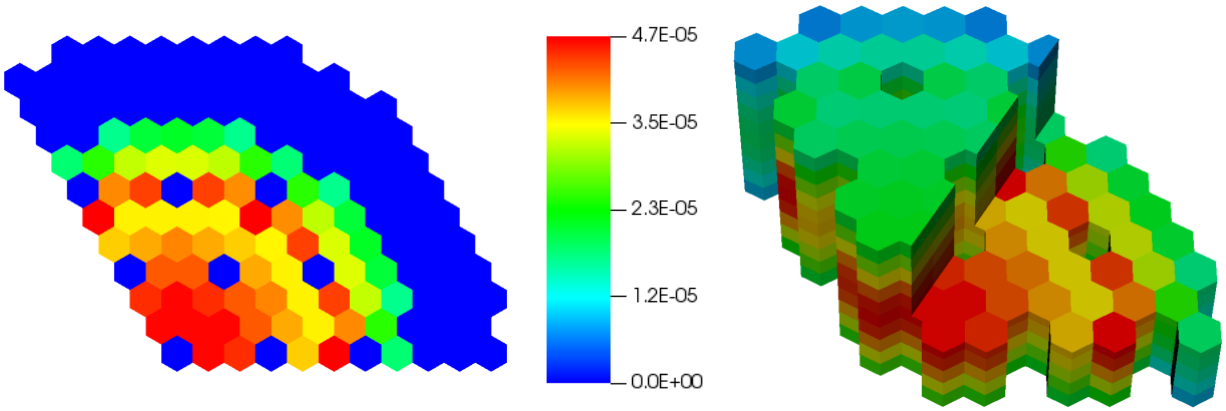

Figure 4-3. Distribution of fuel density coefficient (Δk/k-kg) throughout the core (right) and on a radial slice at z=200cm (left).

Table 4-8. Fuel density coefficient (Δk/k-kg) in each orifice zone.

	Fuel Assembly Orifice Zone					
Height (m)	**1**	**2**	**3**	**4**	**5**	**6**
0.3576	0	0	0	0	0	0
1.6092	0	0	0	0	0	0
1.7808	2.80E-05	2.78E-05	2.66E-05	2.26E-05	2.00E-05	1.10E-05
1.9524	4.08E-05	3.97E-05	3.80E-05	3.26E-05	2.89E-05	1.70E-05
2.124	4.48E-05	4.34E-05	4.15E-05	3.58E-05	3.19E-05	1.90E-05
2.2956	3.79E-05	3.67E-05	3.51E-05	3.04E-05	2.70E-05	1.60E-05
2.4674	2.41E-05	2.36E-05	2.27E-05	1.95E-05	1.73E-05	9.59E-06
2.668	5.45E-06	4.12E-06	4.78E-06	3.28E-06	2.69E-06	2.79E-07
3.6781	0	0	0	0	0	0
4.802	0	0	0	0	0	0

Similar to the sensitivity study performed in Section 4.2.2 for the sodium density coefficient, a sensitivity analysis was carried out to show the impact of the perturbation calculation methodology used in PERSENT on the fuels coefficient, and the results are compiled in Table 4-9. Global Fuel . Similar observations to the one pointed out in Section 4.2.2 can be applied to the fuel density coefficient. The main conclusion is that the first order perturbation calculation provides a reactivity worth that is consistent with the one obtained using exact perturbation theory for small reactivity effect (less than 5%). The verification of the first order perturbation methodology is not performed for the other density coefficients (structure) since similar results are expected.

Table 4-9. Global Fuel Density Coefficient Results for Different Perturbations

PERSENT methodology	Density Factor	Worth pcm/kg
First order perturbation where cross sections are not updated	0.999 0.99 0.95	2.67 2.67 2.67
Exact perturbation where cross sections are not updated	0.999 0.99 0.95	2.67 2.70 2.80
Exact perturbation where cross sections are updated	0.999 0.99 0.95	2.71 2.74 2.85

4.2.5 Structure density coefficient

The structure density reactivity coefficient is obtained using a similar method as the fuel density coefficient. The densities of all structural materials made of HT9 and B_4C, including the duct, cladding, and wire wrap, are multiplied by 0.99 in all regions (driver fuel, upper and lower reflector, radial reflector, control rods, and shielding). The geometry and density of all other components in the core are unchanged. Structure density reactivity coefficients were calculated using the first order perturbation theory of PERSENT without updating the multi-group cross-sections. The resulting reactivity coefficient is a change in reactivity per unit mass of structure in ($\Delta k/k$-kg).

The total structure coefficient is +26.2 pcm/%, which corresponds to +0.036 pcm/K when the linear thermal expansion coefficient of HT9 is used. The 3D distribution of the structure density coefficient is shown in Figure 4-4 and the results for each channel are shown in Table 4-10. The structure density coefficient is positive (in pcm) inside the driver fuel regions as reduced HT9 concentration led to reduced neutron absorption and increased k_{eff}. On the other hand, this coefficient is negative (in pcm) in the upper and radial regions as reduced HT9 concentrations lead to reduced neutron reflection and k_{eff}.

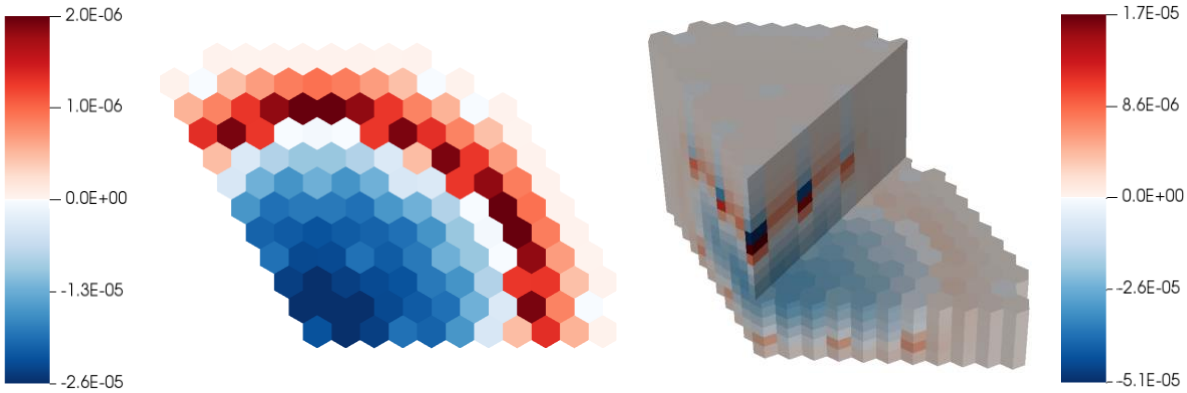

Figure 4-4. Distribution of structure density coefficient (Δk/k-kg) throughout the core (right) and on a radial slice at z=200cm (left).

Table 4-10. Structure density coefficient (Δk/k-kg) in each orifice zone.

Fuel Assembly Orifice Zone						
Height (m)	**1**	**2**	**3**	**4**	**5**	**6**
0.3576	4.90E-12	6.09E-12	5.71E-12	4.38E-12	3.89E-12	1.73E-12
1.6092	1.83E-07	1.42E-07	1.49E-07	1.81E-07	1.78E-07	1.55E-07
1.7808	-3.69E-06	-4.67E-06	-4.32E-06	-2.95E-06	-2.24E-06	1.54E-06
1.9524	-1.46E-05	-1.70E-05	-1.59E-05	-1.26E-05	-1.06E-05	6.91E-07
2.124	-1.80E-05	-2.06E-05	-1.94E-05	-1.55E-05	-1.32E-05	4.20E-07
2.2956	-1.24E-05	-1.41E-05	-1.33E-05	-1.07E-05	-9.00E-06	7.04E-07
2.4674	-6.29E-07	-9.78E-07	-8.24E-07	-5.01E-07	-2.71E-07	1.42E-06
2.668	3.93E-06	4.13E-06	4.13E-06	3.36E-06	3.08E-06	1.35E-06
3.6781	3.16E-07	3.51E-07	3.46E-07	2.70E-07	2.61E-07	1.25E-07
4.802	4.06E-11	4.42E-11	4.24E-11	3.88E-11	3.88E-11	3.21E-11

Control Rod Orifice Zone		Shielding and Reflectors Orifice Zone							
Height	**7**	**Height**	**8**	**9**	**10**	**11**	**12**	**13**	**14**
0.3576	4.64E-12	**0.3576**	1.29E-12	1.04E-12	6.40E-13	4.04E-13	4.34E-13	3.91E-13	1.32E-13
1.6092	2.25E-07	**1.6092**	1.02E-07	8.58E-08	4.40E-08	2.50E-08	2.96E-08	2.31E-08	6.19E-09
2.4674	-3.00E-06	**3.6781**	6.71E-07	6.46E-07	3.21E-07	1.43E-07	2.27E-07	1.62E-07	8.98E-09
3.335	-5.61E-06	**4.802**	1.64E-11	1.58E-11	6.83E-12	2.76E-12	3.69E-12	2.59E-12	5.15E-13
4.802	7.56E-10								

4.2.6 Fuel Doppler (flooded and non-flooded) coefficients

The reference (flooded) fuel Doppler coefficient is calculated by doubling the temperature of the fuel (fuel, zirconium, and fission products), from 807K to 1614K. This coefficient is calculated using the first order perturbation theory option of PERSENT and the cross-sections have to be updated because of the different temperature evaluations. The Doppler coefficient is obtained using the following formula:

$$\alpha_{Doppler}[pcm] = \frac{\Delta\rho\ [pcm]}{\ln\left(\frac{T_f'[K]}{T_f[K]}\right)}$$

where T_f and T_f' are averaged fuel temperatures at nominal and perturbed states [in Kelvin], respectively, which are 807 K and 1614 K, respectively.

SAS4A/SASSYS-1 accounts for the effect of sodium voiding on the Doppler reactivity feedback effect, so a second set of Doppler coefficients was generated for the voided configuration

as described in Section 4.2.3. As with the flooded calculations, fuel temperatures were doubled, with the difference being that the density of flowing sodium in and above the active core section of the fuel assemblies is voided by multiplying by 10^{-10}. A new set of cross-sections is required for the base voided state and the perturbed state (higher temperatures).

The total flooded and voided Doppler constants are -393 pcm and -265 pcm, respectively. The 3D distribution of the flooded Doppler coefficient is shown in Figure 4-5 and the distribution in each axial region within the different thermal-hydraulic channels is provided in Table 4-11. The Doppler coefficient is always negative for this core, but the voided configuration has a less negative coefficient as the flux spectrum is harder.

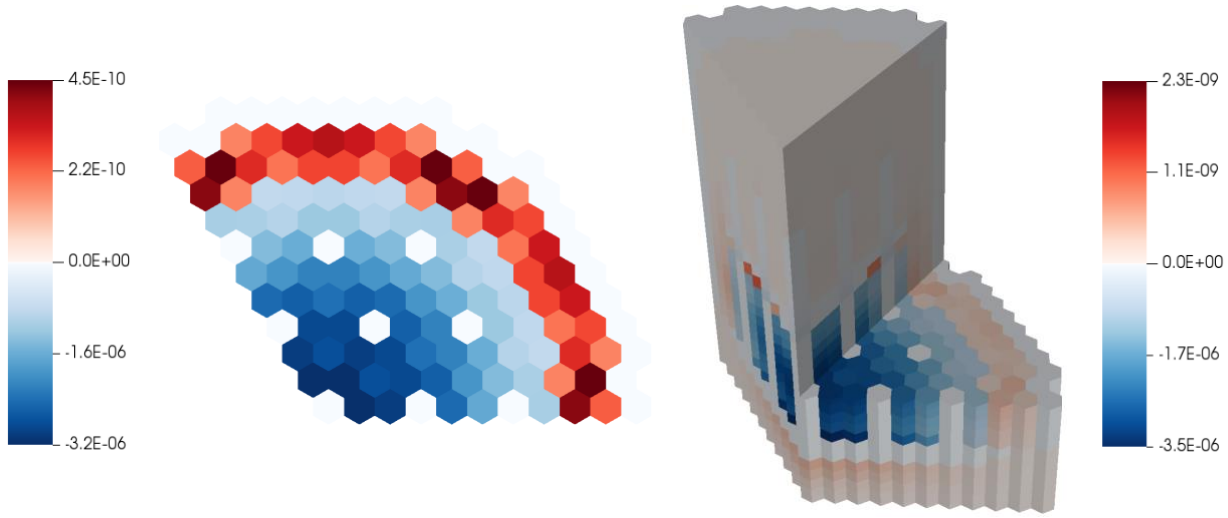

Figure 4-5. Distribution of flooded Doppler coefficient (Δk/k) throughout the core (right) and on a radial slice at z=200cm (left).

The SAS4A/SASSYS-1 code only accounts for the Doppler effect of the Fuel, neglecting the Doppler effect of structure and coolant. A sensitivity study was performed to check this assumption and the results are summarized in Table 4-12. As can be seen, the Doppler effect that would come from HT9, sodium and B_4C has a non-trivial magnitude of -115 pcm, which is ~15% of the total Doppler when the fuel and non-fuel Doppler are combined. As was the case with the fuel Doppler, the non-fuel Doppler is also negative as an increased temperature leads to increased neutron absorption in the resonance region. Neglecting the structure Doppler is justifiable in SAS4A as the temperature changes within the structure for the postulated accidents are typically much smaller than those observed in the fuel (smaller temperature gradient), and the density change dominates the Doppler absorption. The use of the EP versus the FOP impact less than 4% the magnitude of the Doppler result obtained.

Table 4-11. Flooded Doppler constant (Δk/k) in each orifice zone.

Fuel Assembly Orifice Zone						
Height (m)	**1**	**2**	**3**	**4**	**5**	**6**
0.3576	-2.36E-13	-2.07E-13	-1.92E-13	-3.77E-13	-2.77E-13	-1.00E-13
1.6092	-4.60E-08	-3.88E-08	-3.70E-08	-7.61E-08	-5.87E-08	-2.16E-08
1.7808	-1.37E-04	-1.22E-04	-1.20E-04	-2.31E-04	-1.77E-04	-7.46E-05
1.9524	-1.30E-04	-1.16E-04	-1.16E-04	-2.23E-04	-1.73E-04	-8.31E-05
2.124	-1.37E-04	-1.22E-04	-1.21E-04	-2.36E-04	-1.84E-04	-9.07E-05
2.2956	-1.13E-04	-1.00E-04	-9.98E-05	-1.95E-04	-1.53E-04	-7.70E-05
2.4674	-8.70E-05	-7.77E-05	-7.52E-05	-1.53E-04	-1.23E-04	-6.30E-05
2.668	-8.77E-08	-7.10E-08	-8.82E-08	-9.32E-08	-6.30E-08	-4.04E-08
3.6781	4.42E-09	3.24E-09	3.53E-09	7.54E-09	6.46E-09	4.00E-09
4.802	1.44E-11	1.31E-11	1.24E-11	2.43E-11	1.86E-11	6.68E-12

Control Rod Orifice Zone		Shielding and Reflectors Orifice Zone							
Height	**7**	**Height**	**8**	**9**	**10**	**11**	**12**	**13**	**14**
0.3576	-1.66E-13	**0.3576**	-2.37E-14	-3.62E-14	-2.21E-14	0.00E+00	0.00E+00	0.00E+00	0.00E+00
1.6092	-3.51E-08	**1.6092**	-8.37E-10	7.33E-12	2.29E-09	2.34E-09	3.30E-09	1.34E-09	1.69E-10
2.4674	-6.68E-07	**3.6781**	3.24E-08	7.94E-08	8.23E-08	6.63E-08	1.18E-07	4.54E-08	-1.60E-10
3.335	-1.56E-05	**4.802**	1.03E-12	1.59E-12	6.61E-13	8.77E-14	1.86E-13	7.10E-16	0.00E+00
4.802	1.95E-09								

Table 4-12. Sensitivity analysis on the Doppler effect.

	Doppler Constant [pcm]
Fuel Doppler First order perturbation	-393
Fuel Doppler Exact perturbation	-379
Non-Fuel Doppler First order perturbation	-115

4.2.7 Axial expansion coefficient

The axial expansion reactivity feedback coefficient is calculated by increasing the height of the active core of the fuel assemblies by 1%, which corresponds to a 1% fuel volume increase. All of the regions above the active core are translated upwards consistent with the dimensional change

of the active core. To conserve mass, the densities of all solid materials (fuel and HT9) in the expanded active core are reduced by 1% while the sodium density is not changed.

To prevent the axial expansion coefficient from including aspects of control rod insertion, the control rod tips are axially shifted upwards so that they remain parked at the upper edge of the active core (same relative distance as the base state). As stated previously, this coefficient is computed with DIF3D and not PERSENT and the multi-group cross-sections are not updated for the perturbed state.

The resulting axial expansion coefficient represents the reactivity feedback due to uniform axial expansion of the active core. The total axial expansion coefficient is -135 pcm/%, which translates to -0.185 pcm/K when applying the thermal expansion coefficient of HT9. The thermal expansion coefficient of HT9 is used as the metallic fuel is assumed to have swelled and is frictionally locked to the cladding at EOC. It should be noted that SAS4A/SASSYS-1 does not use this coefficient as it models the axial expansion by combining the fuel, structure and coolant density coefficients discussed earlier.

4.2.8 Radial expansion coefficient

The radial expansion reactivity feedback coefficient is calculated using DIF3D, on the base and perturbed states with no cross section updates. The radial expansion reactivity coefficient is defined by increasing the pitch of all assemblies by 1%, while conserving the mass of solid materials in the modeled problem (sodium mass is the only component not conserved). There are two slightly different approaches that can be used for defining the perturbed state:

- **Approach 1**

The traditional approach applied at ANL considers a uniform expansion of the homogeneously defined fuel assembly and movement with respect to grid plate changes, leading to increased volume fractions for the fuel, structure and coolant by 0.980296. In this approach, the densities of all solid materials present in the core are multiplied by a factor of 0.980296, corresponding to $(1/1.01)^2$, or the inverse of the volumetric change in each assembly position. The density of sodium is not changed as the system is assumed to backfill the extra volume with flowing sodium. The resulting coefficient, in units of $\frac{\Delta k/k}{\%\ \text{change pitch}}$, represents the reactivity feedback due to uniform thermal expansion of the fuel combined with translation due to the grid plate. This approach yields a reactivity coefficient of -604 pcm/% which translates to -1.05 pcm/K when using the linear expansion coefficient of SS-316. With this approach, the sodium mass in the core is increased by 85kg (120 degree periodic core model), and the mass of other solid elements are unchanged.

- **Approach 2**

The alternative approach considers no expansion of the explicitly defined fuel assembly, but only a 1% change in the assembly pitch corresponding to movement with respect to grid plate changes and resulting to increase in inter-assembly sodium gap. This approach automatically considers mass conservation for the fuels and structure, as the volume and densities of solid material are maintained. However, this approach differs from #1 as the resulting sodium volume fraction is increased due to increased inter-assembly gap. This approach yields a reactivity coefficient of -655 pcm/% or -1.14 pcm/K assuming linear expansion coefficient of SS-316. It is more negative than Approach #1 due to increased Na content in expended configuration, which is

associated with overall negative reactivity effect as shown in Section 4.2.2. Through this approach, the sodium mass in the core is increased by 232kg (120 degree periodic core model), and none of mass of other elements are changed.

To summarize, both approaches consider increased assembly pitch, but approach 1 considers the radial expansion of the assembly duct and pins so the sodium volume fraction is smaller than that for approach 2 that retains the assembly dimension. The different approaches used for radial expansion coefficient calculation led to ~8% in difference in the radial expansion coefficient. Both approaches are valid for generating radial expansion coefficient to SAS4A but the first approach is still preferred because it models the radial expansion of the structures internal of the assembly may have on displacing sodium, which are not otherwise being considered in the SAS model.

4.2.9 Control rod driveline worth

The worth for the control rods is calculated by inserting all of the control and safety rods. In the base state, all of the control rod tips are parked at the top of the active core. In the perturbed state, the control rod tips are parked 5 cm below the top of the active core. This calculation is only done to for benchmarking purposes. More detailed information required by SAS4A involves S-curve for control rods (N and N-1) and safety rods, together with rod positions. Those are being provided in Section 5. Control rod driveline calculations are performed using DIF3D, rather than PERSENT, and the cross-sections in the perturbed state are not updated. The insertion worth is calculated to be -241 pcm which represents -48.1 pcm/cm of rod insertion.

4.3 Power Distribution Calculations

The total power distribution is calculated by DIF3D/VARIANT and GAMSOR on the 120 degree periodic core geometry described earlier. As indicated in Table 3-1, the approach used for generating multi-group cross-sections for the power is simplified when using GAMSOR where the TWODANT step is not utilized. Because DIF3D-VARIANT defines full hexagons in its output, the comparison should be careful to account for DIF3D reporting the central assembly integrated reaction rates such as power consistent with that of a full core model instead of the 120 periodic.

The neutron, gamma, and total power distribution in the active core are shown in Figure 4-6. As can be seen, the gamma power is small relative to the neutron power. Relative plots of the neutron and gamma power distributions are also included to display the differences in spatial distribution of the two power components. The axial power for each orifice zone from the full core model is provided in Table 4-13 while the axially integrated power distribution is displayed in Figure 4-6. The total power predicted by GAMSOR is 1000 MW and ~12.2% of that power is from gamma heating.

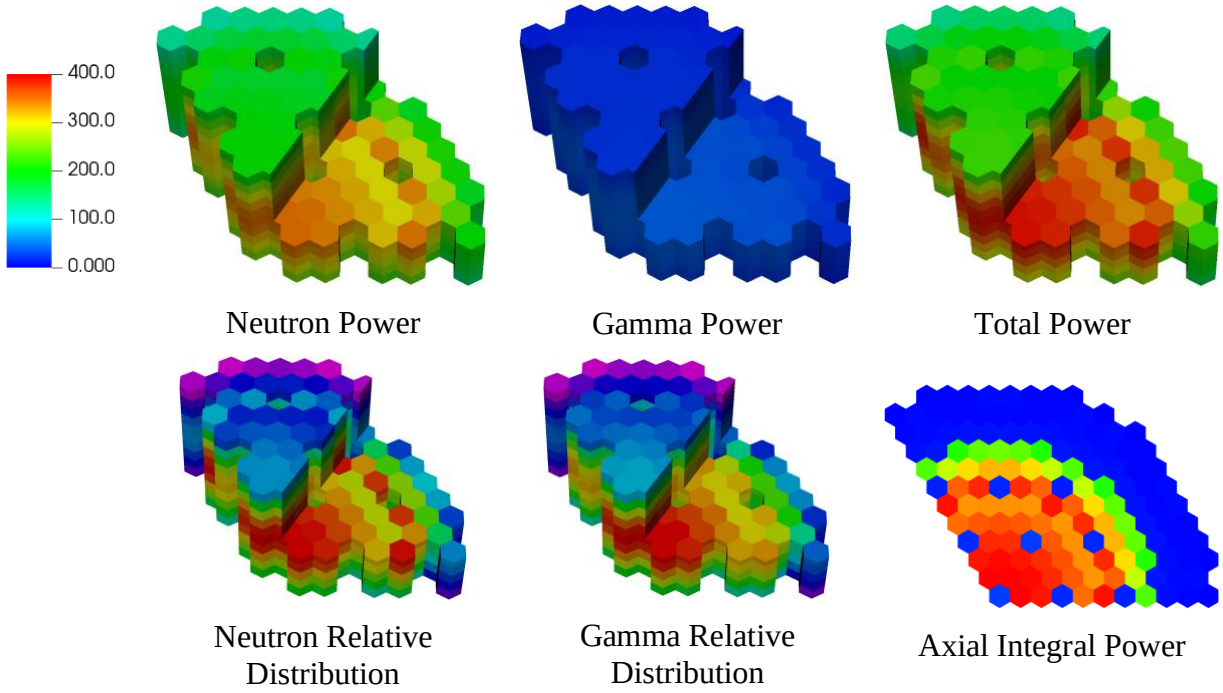

Figure 4-6. Gamma (left) and Neutron (right) power distributions provided in (W/cm^3).

Table 4-13. Total Power (W) in each orifice zone (for the full-core).

Fuel Assembly Orifice Zone						
Height (m)	**1**	**2**	**3**	**4**	**5**	**6**
0.3576	5.22E+03	4.43E+03	4.27E+03	9.13E+03	7.42E+03	4.45E+03
1.6092	1.21E+06	1.00E+06	9.74E+05	2.11E+06	1.72E+06	1.01E+06
1.7808	2.77E+07	2.05E+07	2.01E+07	4.56E+07	3.66E+07	2.42E+07
1.9524	3.39E+07	2.50E+07	2.45E+07	5.60E+07	4.49E+07	2.93E+07
2.124	3.58E+07	2.63E+07	2.58E+07	5.92E+07	4.76E+07	3.11E+07
2.2956	3.23E+07	2.37E+07	2.32E+07	5.35E+07	4.30E+07	2.85E+07
2.4674	2.41E+07	1.76E+07	1.72E+07	4.00E+07	3.23E+07	2.25E+07
2.668	2.54E+05	1.97E+05	1.98E+05	4.44E+05	3.57E+05	2.27E+05
3.6781	2.53E+05	1.93E+05	2.01E+05	4.40E+05	3.37E+05	2.39E+05
4.802	4.46E+04	3.67E+04	3.59E+04	7.88E+04	6.38E+04	3.73E+04

Control Rod Orifice Zone		**Shielding and Reflectors Orifice Zone**							
Height	**7**	**Height**	**8**	**9**	**10**	**11**	**12**	**13**	**14**
0.3576	3.99E+03	**0.3576**	1.26E+03	2.18E+03	1.84E+03	1.38E+03	1.91E+03	8.19E+02	2.56E+02
1.6092	9.15E+05	**1.6092**	2.66E+05	4.54E+05	3.64E+05	2.55E+05	3.64E+05	1.53E+05	3.90E+04
2.4674	1.62E+06	**3.6781**	1.32E+06	2.15E+06	1.99E+06	1.72E+06	1.52E+06	4.41E+05	3.61E+05
3.335	2.49E+06	**4.802**	9.68E+03	1.59E+04	1.18E+04	7.45E+03	1.08E+04	4.31E+03	9.59E+02
4.802	2.94E+04								

5 Shutdown Margin Analysis

The shutdown margin of a reactor is defined as the difference between the available reactivity worth from the control systems and the maximum required reactivity to be controlled [16]. Typical SFRs have two reactivity control systems which may perform different functions and face different reactivity control requirements. Typically, the primary system is needed to shut down the reactor from the Hot Full Power (HFP) state to the Cold Zero Power (CZP) state, so it needs to compensate for the excess reactivity due to fuel burnup, the change in the operating temperature, an overpower fault, a reactivity fault, and uncertainties associated with reactivity burnup swing, fuel fabrication, absorber fabrication, neutron cross section, actual temperature distribution, etc. The secondary control system is typically needed to shut down the reactor to the Hot Zero Power (HZP) condition, and it does not need to compensate for the excess reactivity due to fuel burnup.

The shutdown margin calculations for the ABR-1000 benchmark exercise are simplified from those typical in design calculations. The ABR-1000 model chosen for the comparison study only considers the fuel composition at the End Of an Equilibrium Cycle (EOEC) and no other time point data is considered. The shutdown margin for the EOEC state has different excess reactivity constraints as the ABR-1000 design focused on a near critical system at EOEC. In this scenario, the primary control rod tips are parked at, or near, the top of the active core. Thus, the reactivity fault, typically due to accidental ejection of a control assembly, is effectively zero. A decision was made to focus on calculations of the control system worth (Section 5.2) and the reactivity change due to change in operating temperature (Section 5.3 and 5.4) for this benchmark exercise. The overpower fault and the uncertainties were not evaluated.

5.1 Model Modification

The DIF3D model used for the reactivity feedback calculations was modified to capture the unique features of the shutdown margin calculations. The material compositions were not changed nor was the core loading. The upper and lower structures were defined separately and mapped to different neutron cross section sets. This modification is needed because the upper and lower structures would experience different temperature changes from HFP to HZP. The axial layouts of the modified assembly models are presented in Figure 5-1. The DIF3D model was changed to a full core model instead of using the 120 periodic model. This change is needed to evaluate the control system worth for a single stuck assembly with the highest worth.

The average inlet and outlet coolant temperatures are 628.2K and 783.2K, respectively. The average fuel temperature is 807.2K and it was assigned to all five axial regions of the active core model. The region-wise temperature assignment is listed in Table 5-1 for the HFP state. Several assumptions are involved with this assignment:

1. Lower structures (below the active core, the active control region, the radial reflector, and the radial shield) are set to the core inlet coolant temperature.
2. Upper structures (above the active core, the active control region, the radial reflector, and the radial shield) are set to the core outlet coolant temperature.
3. The structures and coolant in the active core, the active control region, the radial reflector, and the radial shield are set to the average core coolant temperature.
4. The control rod absorber (B_4C) is set to the average core coolant temperature, since the control assemblies are fully withdrawn at EOEC with small heat generation.
5. The average core fuel temperature of 807.2K is used for the fuel material.

6. The sodium bond and the gap sodium between assemblies are assumed to have the same temperature as the average core sodium coolant.

For the HZP condition, no power is being produced, so the inlet and outlet coolant temperature are the same. In this case, all materials, including fuel, were assigned a temperature of 628.2K. Likewise, for the CZP condition, the temperature of all materials was assigned the refueling temperature of 478.2K.

MC^2-3/TWODANT models were developed based on the modified DIF3D model for the HFP condition. The methodology used a two-step procedure similar to that described in Section 3.1.1 but the 1D lattice calculation was not used deferring to 0D models for each assembly. This does not evaluate the self-shielding effect of the absorber rod correctly and consequently affects the control assembly s-curve calculation. OpenMC calculations were also conducted for the control assembly s-curve calculation to resolve this issue.

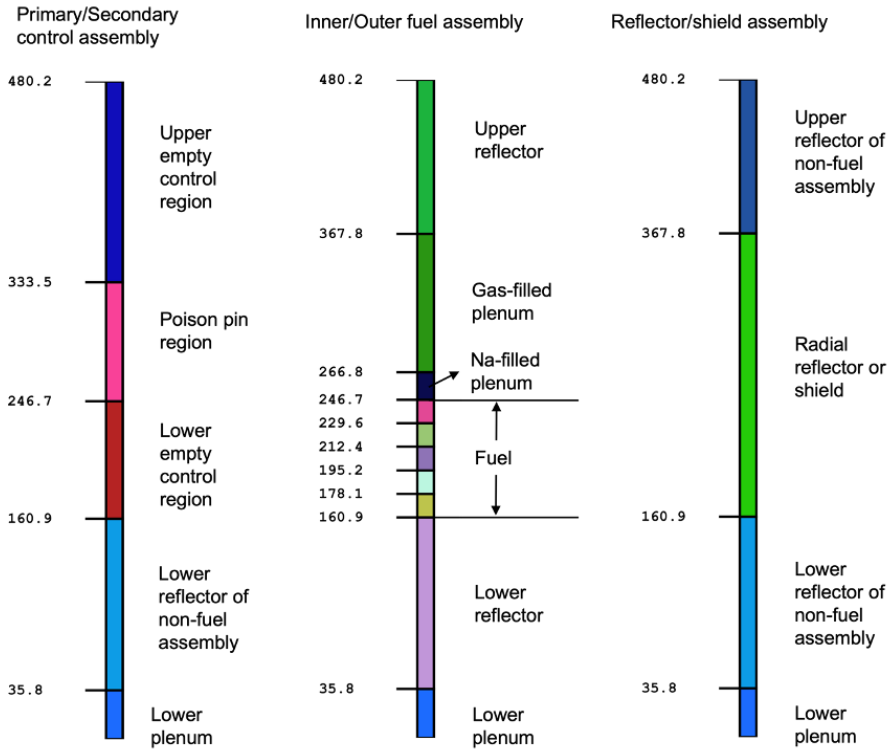

Figure 5-1 Axial assembly layout of the modified ABR-1000 model with dimensions in [cm].

Table 5-1 Material temperature [K] in different regions at the HFP condition.

Region	Fuel/B_4C	Steel	Sodium
Lower plenum	-	628.2	628.2
Lower reflector of non-fuel assembly	-	628.2	628.2
Lower empty control region	-	628.2	628.2
Poison pin region	705.7[1]	705.7	705.7
Upper empty control region	-	783.2	783.2
Lower reflector	-	628.2	628.2
Fuel	807.2	705.7	705.7
Na-filled plenum	-	783.2	783.2
Gas-filled plenum	-	783.2	783.2
Upper reflector	-	783.2	783.2
Radial reflector	-	705.7	705.7
Radial shield		705.7	705.7
Upper reflector of non-fuel assembly	-	783.2	783.2

1. The average coolant temperature = 0.5(inlet temperature + outlet temperature).

5.2 Control System Worth

The control assembly worth was evaluated at the HFP condition. The cross section set generated for the HFP condition was used for all the cases investigated. Two s-curves were generated for each of the primary and secondary control systems in this analysis which are provided in Figure 5-3 and Figure 5-4, respectively. Each figure provides an s-curve for the motion of all assemblies and an s-curve where the highest worth assembly in the control system is stuck. For the primary control system result in Figure 5-3, a single assembly in the fourth hexagon ring was considered stuck, identified in Figure 5-2, for the one_stuck_assembly curve. For the secondary control system result in Figure 5-4, the central control assembly was considered stuck in the one_stuck_assembly curve. Ten control rod positions were used to obtain the s-curve results and the positions and individual s-curve results are provided in Table 5-2.

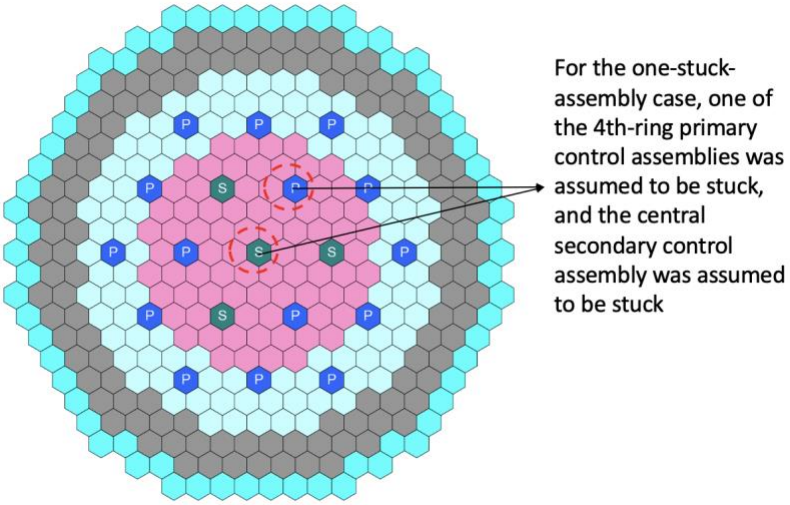

Figure 5-2 The location of the assumed stuck control assembly.

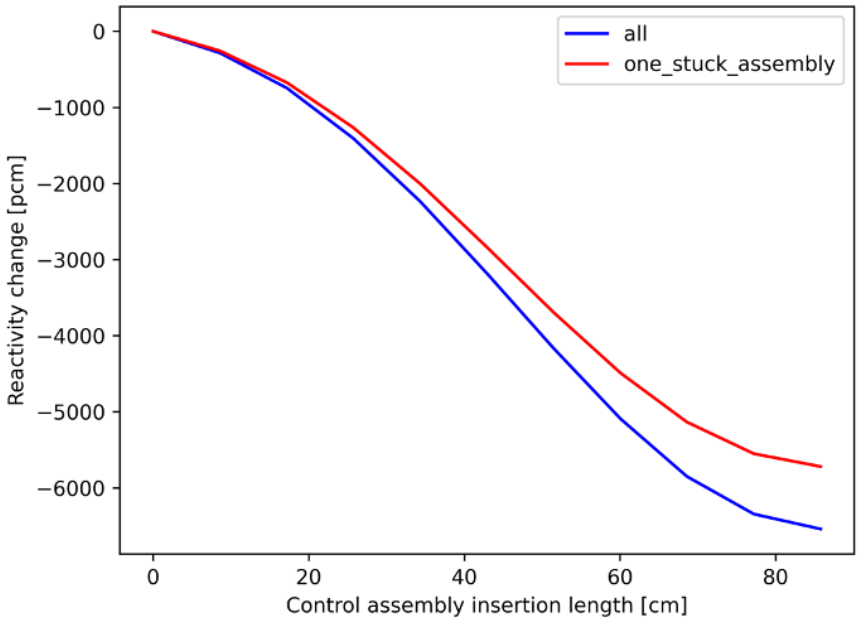

Figure 5-3 The s-curve for the primary control assembly from DIF3D calculation.

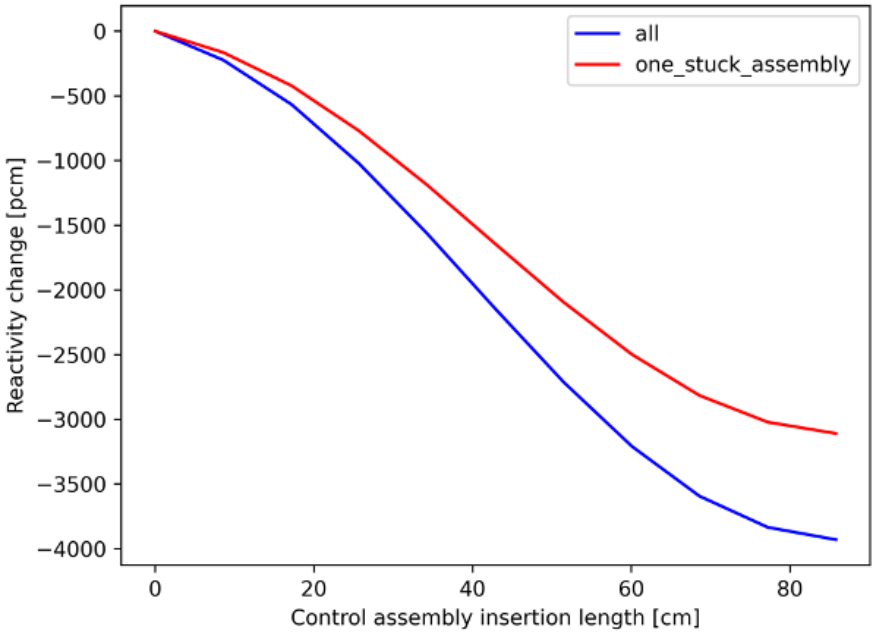

Figure 5-4 The s-curve for the secondary control assembly from DIF3D calculation.

Table 5-2 The reactivity change [pcm] at different insertion lengths of the primary and secondary control assemblies from DIF3D calculation.

Insertion [cm]	Primary control		Secondary control	
	All	One stuck assembly	All	One stuck assembly
85.8	-6541	-5720	-3931	-3110
77.2	-6344	-5551	-3835	-3022
68.6	-5850	-5135	-3594	-2816
60.1	-5095	-4493	-3210	-2499
51.5	-4169	-3697	-2714	-2096
42.9	-3181	-2837	-2148	-1646
34.3	-2233	-2001	-1566	-1190
25.7	-1404	-1263	-1024	-771
17.2	-746	-674	-567	-422
8.6	-285	-257	-224	-165
0	0	0	0	0

To convert the reactivity measure from pcm to dollars, the effective delayed neutron fraction is obtained from Section 4 (330 pcm). The total primary control system worth is $19.9 while the single stuck assembly worth is $17.4. These are ~50% less than that reported in Reference [2] which was traced to a difference in the absorber composition used in the current and the original [2] model. The OpenMC results for the primary and secondary control systems are presented in Figure 5-5 and Figure 5-6. The total primary control system worth is $17.9 while the single stuck assembly worth is $15.9. They are about 10% less than the DIF3D prediction due to the homogenization, which is consistent with observation from Section 3.2.

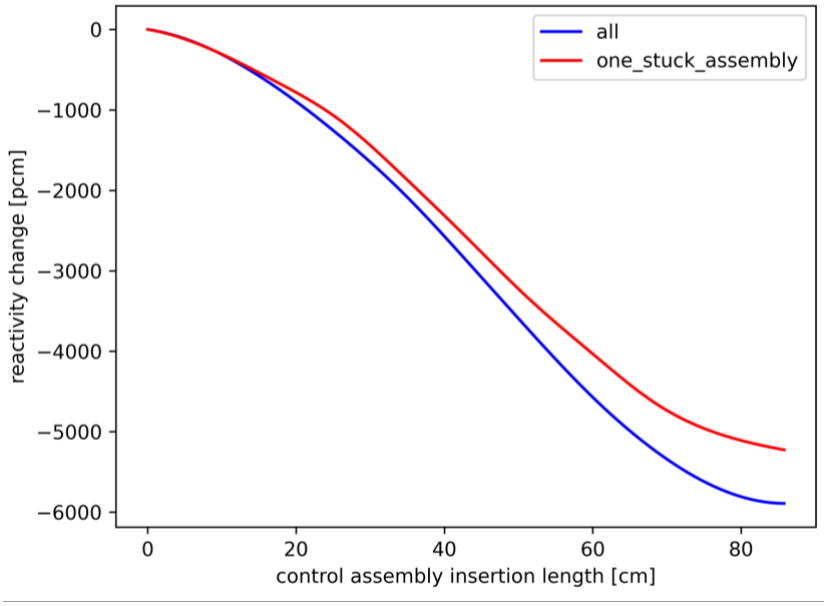

Figure 5-5 The s-curve for the primary control assembly from OpenMC calculation.

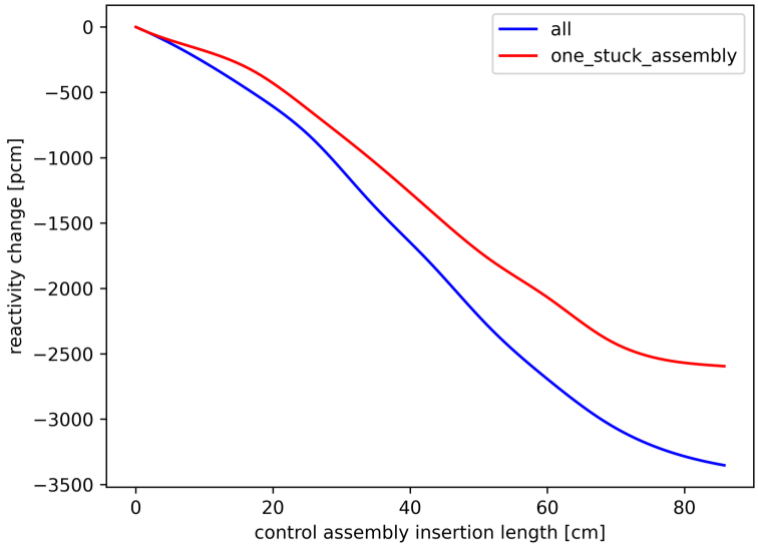

Figure 5-6 The s-curve for the primary control assembly from OpenMC calculation.

5.3 Reactivity Change from HFP to HZP

The reactor power is reduced to zero from the HFP to the HZP operating condition and thus the inlet and outlet coolant temperature can be assumed equal. Similarly, the temperature of all materials in the model can be assumed as the inlet coolant temperature after reaching equilibrium. The important part of this assumption is that the outlet temperature is equal to the inlet coolant temperature even though the actual power level is not zero because of decay heat. This implicitly assumes that the coolant flow rate is sufficiently high to ensure that the inlet and outlet temperature are the same or very similar.

The change in the outlet temperature affects the reactor reactivity through three mechanisms: the coolant densification, the structure/fuel contraction, and Doppler broadening of the neutron cross sections. The correlations for the HT9 linear thermal expansion coefficient and the sodium coolant density are given in Eq. (5.1) and Eq. (5.2), respectively. These two equations were used to assess the structure and density changes due to the reactor state transition.

$$\frac{\Delta L}{L} = -0.2191 + 5.6780 \times 10^{-4}T + 8.1110 \times 10^{-7}T^2 - 2.5760 \times 10^{-10}T^3 \quad (5.1)\ [17, p. 9]$$

$$\rho = 1.0316 - 3.0113 \times 10^{-4}T + 8.0435 \times 10^{-8}T^2 - 3.1162 \times 10^{-11}T^3 \quad (5.2)\ [18]$$

To reiterate, the HFP condition details provided in Table 5-1 are being converted to a uniform temperature and thus materials in those regions are subject to different contractions as they cool to the inlet temperature. One should take note that real shutdown margin calculations would consider a much more rigorous temperature distribution than that defined in Table 5-1 and that the neutronics model would be similarly adjusted. Changes made to the reactor model to account for the temperature change are listed in Table 5-3 along with the corresponding reactivity worth of each change. Each new case in Table 5-3 includes the cumulative impact of all preceding cases and all worth results are done with respect to Case 0. For the former issue, the sodium density change indicated in Case 2 also includes the sodium density changes described in Case 1. This means that Case 7 is the cumulative impact of applying all of the listed changes in case 1-7 to the model.

Inspecting the results in Table 5-3, the reactivity change between Case 1 and Case 0 is negative as an increase in the sodium density in the fuel, reflector, and shield regions leads to a softer spectrum. The negative worth reduces between Case 2 and Case 1 because as the sodium density is increased in the upper structures, the leakage from the reactor is reduced (thus a positive feedback). The combined effect from the sodium density change in Case 1 and 2 is still negative and is consistent with the positive sodium density coefficient reported in [2] and in Section 4.2.2. Moving to Case 3, There is a subtle point for the sodium inside the plenum above the fuel. The coolant sodium mass in the core is not conserved (it is conserved inside the reactor vessel, i.e., the hot sodium level drops when hot pool temperature drops), but the sodium mass inside the plenum should be conserved. Thus, when the sodium density increases, the sodium-filled plenum height would decrease. Its effect on the reactivity is small when comparing Case 3 and 2.

Case 4 and Case 5 evaluate the reactivity change due to axial contraction. The change is cumulatively positive when comparing to Case 3 and is consistent with the axial expansion coefficient in [2]. The axial contraction of the fuel region approximately counterbalances the reactivity change due to sodium densification. The contraction of structural regions has little effect on the core reactivity (< 1 pcm) as they are outside the high-worth active fuel regions. The large positive reactivity difference between Case 5 and 6 is mainly due to the fuel Doppler broadening.

The effect of radial contraction on the core reactivity cannot be evaluated using DIF3D. When transitioning from the HFP to HZP condition, the assembly pitch does not change in the lower part of an assembly, but changes in the heating region and the upper part of the assembly. The DIF3D code only allows a single assembly pitch in a model and thus the radial expansion and contraction cannot be modeled explicitly. For this reason, the radial expansion coefficient (-0.31 cents/K) is used to assess the worth of the radial contraction. Only the upper half of the core is subject to radial contraction, so the reactivity change was divided by two, and this corresponds to

a positive reactivity change of 78.8 pcm. Combined with the changes due to sodium densification, axial contraction, and fuel Doppler, the net reactivity change from the HFP to the HZP condition is 0.53$.

The purpose of the shutdown margin calculation is to ensure that the control systems provide sufficient margin when the reactor is shutdown. An additional calculation (Case 7) was performed with all of the primary control assemblies fully inserted. The result was compared to the reference case (Case 0) with all the primary control assemblies fully inserted. Thus, this case may represent the real shutdown margin more closely.

Table 5-3 The reactivity change from the HFP to HZP condition.

Case No.	Changes from previous case	[pcm]
0	Reference case at the HFP condition	-
1	Increase Na density in fuel, radial reflector/shield	-42.04
2	Increase Na density in upper structures	-20.51
3	Reduce Na plenum height	-26.38
4	Reduce fuel, radial reflector/shield height	-7.79
5	Reduce Na/gas plenum, upper structures height	-6.81
6	Use of updated neutron cross section with HZP temperature	94.15
7	Fully insert all primary control assemblies	83.33*

* Compared with Case 0 with all primary control assemblies fully inserted.

5.4 Reactivity Change from HZP to CZP

The reactivity change from the HZP to CZP condition was assessed in a similar approach as that described in Section 5.3. The changes were introduced stepwise to the reference case, which is Case 6 in the HFP-to-HZP calculation. The changes were added cumulatively on top of the reference case. The detailed changes are listed in Table 5-4 along with the corresponding reactivity change. The radial contraction can be evaluated with DIF3D by reducing the assembly pitch since the temperature change in all regions is the same (from the coolant inlet temperature to the refueling temperature). The radial contraction and the fuel Doppler broadening cause the largest reactivity changes, which is similar to the HFP-to-HZP case. The sodium densification yields a negative reactivity change due to a softer spectrum while the axial contraction yields a positive impact on reactivity. The net reactivity change from the HZP to CZP condition is 0.63$. This is slightly larger than that of transitioning from the HFP to HZP condition because of the change in lower structures.

Table 5-4 The reactivity change from the HZP to CZP condition

Case No.	Changes from previous case	[pcm]
6	Reference case at the HZP condition (Case 6 in Table 5-3)	-
8	Reduce assembly pitch	109.93
9	Increase Na density in all regions	46.56
10	Reduce the axial dimension of all regions	73.87
11	Use of updated neutron cross section with CZP temperature	208.23

12	Fully insert all primary control assemblies	182.86*

* Compared with Case 0 with all primary control assemblies fully inserted.

5.5 Summary

The shutdown margin was calculated based upon the control worth and reactivity change calculated and discussed in Section 5.2 to 5.4. A summary of the results is listed in Table 5-5. A large difference is observable for the control worth of the primary control system from that in reference [2] which is traceable to different control assembly compositions. This difference was made intentionally [1]. The benchmark model described in [1] that was used in this work was developed based on the original ABR model [2] but with the control rod composition modified to reduce the shutdown margins down to a more realistic level. The shutdown margin results are compared to the original ABR report [2] since there no shutdown margin calculations were proposed in the OECD/NEA benchmark exercise [1]. Due to the difference in the two models, the control rod worth is different, but other parameters agree well. Regardless, this change does not affect the purpose of this analysis which is to demonstrate the shutdown margin evaluation. The secondary control system is typically required to shut down the reactor to the HZP condition [16], so the HZP-to-CZP reactivity change should not be included. This was included in this study to be consistent with Ref. [2] and thus assumes an additional requirement is posed on the secondary control system.

Table 5-5 Shutdown margin evaluation for the secondary and primary control systems.

Parameter	Primary control [$]		Secondary control [$]	
	Ref. [2]	Calculated	Ref. [2]	Calculated
Control worth	40.2	19.9	10.4	11.9
Worth with One Stuck Assembly	35.5	17.4	7.6	9.4
HFP to HZP	0.54	0.53	-	0.54
HZP to CZP	0.66	0.63	-	0.63
Shutdown margin*	-	16.21	-	8.29

* The shutdown margins of the two cases are not directly comparable due to the difference in the primary control assembly model and the intentional exclusion of the uncertainty and overpower fault in the current study.

.

6 Pin Power Reconstruction Analysis

For fast spectrum reactors, the methodology encompassed by DIF3D [6][19][10][11],REBUS [20], GAMSOR [7], and PERSENT [8] relies upon homogenized assembly details where the multi-group cross section methodology is focused on preserving the reaction rates between the homogeneous geometry and the originating heterogeneous one. From this viewpoint, performing fuel cycle analysis in the homogenized geometry should closely reproduce the desired assembly average depletion results. The peaks of course are not necessarily ensured in this transformation, and thus the greater the flux gradient across the assembly, the worse the error becomes as the cross section methodology simply cannot capture it noting that this error may still be small for most applications.

In thermal spectrum reactors, the lattice calculation (MC^2-3 equivalent) is typically used with the global flux gradient (DIF3D equivalent) to "reconstruct" the pin level reaction rates (such as power). This is important as the pin peaking in the lattice calculation can be remarkably different. Fortunately, for fast spectrum reactors that target electrical power production, the pin peaking in the fuel assembly lattice calculation is relatively unimportant ranging from peak to average values of 0.99 to 1.01, if not a smaller range. In this scenario, evaluation of the fuel pin power just using the global gradient is sufficient to produce the pin level reaction rates with the accuracy limitations of the homogenized methodology stated previously. It is important to note that there can be some cases where pin power reconstruction factors are necessary such as experimental assemblies loaded with differently enriched pins and fuel types and some control rod assemblies where spatial self-shielding can alter the power reconstruction.

Figure 6-1 shows the axially integrated assembly power distribution in the left picture and the axially integrated pin power distribution from DASSH on the right hand picture for the chosen study problem ABR-1000.

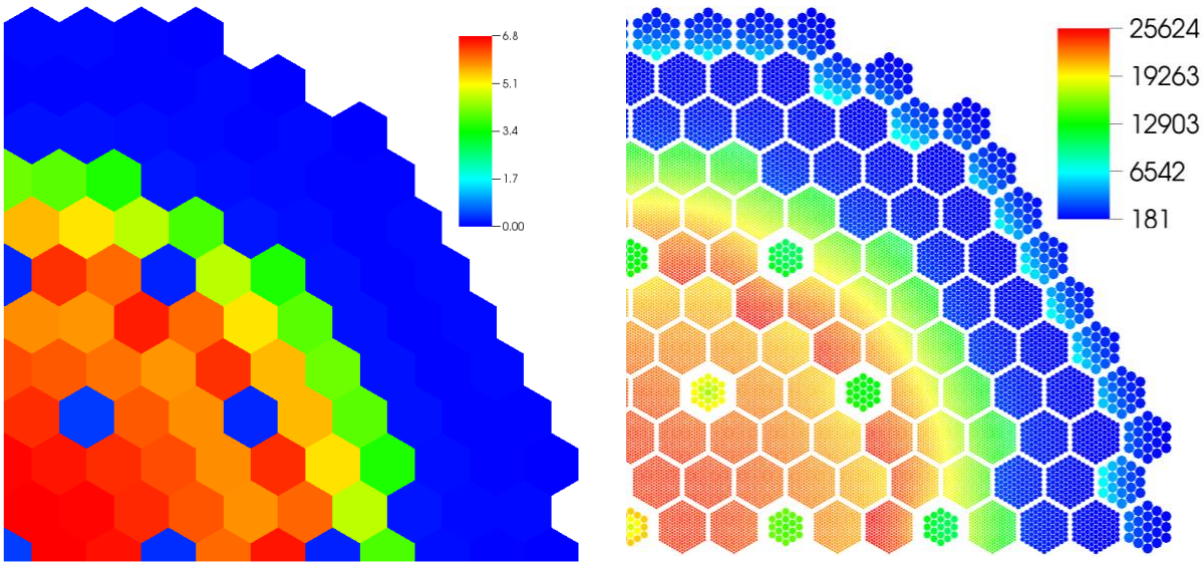

Assembly Power (MW)

Pin Power (W)

Figure 6-1. Axially integrated assembly and DASSH pin power for ABR-1000.

In Figure 6-1, the pin power details mimic the assembly power details but the global gradients are clearly more visible in the pin power picture. This is of course not a surprise as the pin power distribution was normalized to be consistent with the assembly power picture. This normalization is the requirement of any de-homogenization procedure or pin power reconstruction algorithm.

The pin power distribution is important for the fluid flow and temperature evaluation within each assembly. Sodium cooled fast reactors almost always assume ducted assemblies and this allows the flow rate and thus temperatures to be constrained in the domain by assembly position. Those assemblies with a flat pin power distribution, such as those in rings 2 and 3, turn out to not be as important as those with steep gradients, such as those in ring 8. This is primarily because coolant mixing in the assembly over the active core height is not perfect and thus the temperature gradient across the assembly is much greater in the assemblies in ring 8 than in rings 2 and 3. This can require increases in the coolant flow rate in such lower power assemblies which can reduce the efficiency of the power plant. Consequently, the assemblies with steep gradients tend to be more important and thus obtaining accurate pin power distributions tends to be an important requirement on the neutronics component.

6.1 DIF3D Pin Power Reconstruction Techniques

The DIF3D code has three solver options: DIF3D-FD [6], DIF3D-Nodal [19], and DIF3D-VARIANT [10][11]. In previous work, a pin power reconstruction methodology was developed for DIF3D-FD as part of SE2ANL [21]. Similarly, a pin power reconstruction methodology was developed for DIF3D-Nodal as part of RCT [22]. Because the RCT methodology uses average volumetric and surface quantities from the solver, DIF3D-VARIANT can also be used in RCT using the same pin power reconstruction methodology as DIF3D-Nodal. Finally, the more recent efforts at ANL have focused on using a more rigorous power distribution methodology as part of DASSH.

In the 3D multi-group solvers DIF3D-Nodal and DIF3D-VARIANT, a high order methodology is used in each mesh and spatial discontinuities are introduced at the node surfaces to avoid requiring extreme spatial expansions. These discontinuities allow the current to be held accurate and thus the mesh-wise reaction rates to be preserved at the expense of “inaccurate” flux levels near the boundaries of each mesh. With most reactor problems, the discontinuities amount to a fourth (or less) significant digit difference in the scalar flux at the interface between two adjacent assemblies. Clearly this is not inaccurate, but for some extreme reactor problems, the discontinuities can impact the first significant digit and thus the discontinuities can become a problem. With mesh refinement and/or a basis expansion, such discontinuities can be resolved and these problems can be diminished or eliminated.

For the ABR-1000 study problem, the axial flux discontinuities are negligible when using the base 6^{th} order flux and 1^{st} order leakage approximation in DIF3D-VARIANT and thus pushing the flux or leakage to higher order values is rather unnecessary. In the remainder of this document, any spatial discontinuities observed can be assumed to arise from compositional differences between adjacent meshes where this is expected from the underlying modeling methodology although not consistent with the reality of a real reactor system where atom density changes are smooth. The secondary reason for observed discontinuities is because of how energy is assumed to be preserved when converting the homogeneous representation into the heterogeneous one (mesh-wise energy conservation).

6.1.1 DIF3D-FD Methodology for SE2ANL

Figure 6-2 shows the triangular mesh associated with DIF3D-FD where each hexagon is broken into 6 triangles. The pin power fitting methodology assumes that the radial pin power distribution is independent of the axial position. The radial pin power distribution is determined at the core mid-plane and uses the 6-term monomial expansion shown at the bottom of Figure 6-2. The fitting procedure considers the six triangles of each assembly along with the adjacent 18 triangles as shown (the large black hexagon in Figure 6-2 consists of 24 triangles).

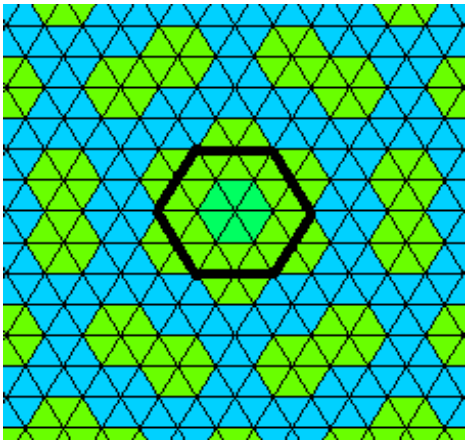

$$\bar{f}^T(x,y) = [1, x, y, xy, x^2, y^2]$$

$$P_g(x,y) = \bar{f}^T(x,y) * \bar{p}_g$$

Figure 6-2. DIF3D-FD radial fitting algorithm for pin powers

The fitting is done on each group flux to produce a set coefficients $\bar{p}_g$ for that group. These are combined with the heating factors to produce a radial power shape. The power shape is evaluated at the (x,y) coordinate centers of each pin and the result is normalized to yield pin power factors (that sum to unity) for each assembly. Axially, the assembly power is stored for every axial mesh (~2-5 cm meshing is used in DIF3D-FD). Linear interpolation is used between mesh centroids in the domain to obtain the power deposited in each mesh used in Superenergy-2 (typically < 0.5 cm meshing is used). This axial power term is combined with the pin factors to produce the power for each pin in each axial TH mesh.

6.1.2 DIF3D-Nodal and DIF3D-VARIANT Methodology for RCT

For DIF3D-Nodal, a transverse integrated formulation is used which allows an accurate and very computationally efficient solver (compared with DIF3D-FD) for reactor problems based upon a homogenized assembly methodology. However, the DIF3D-Nodal formulation prevents a rigorous flux reconstruction from being used as it does not introduce a rigorous 3D basis. RCT gets around this weakness by defining the flux reconstruction using what is available in the DIF3D-Nodal flux solution which includes both surface and volumetric quantities. Figure 6-3 shows the typical flux and current moments on each surface (s1, s2, … represent surface flux moments) and the corner fluxes (c1, c2, …). The corner fluxes are obtained by combining the flux details from

three adjacent hexagons as shown in the right picture of Figure 6-3. In total, the RCT flux fitting considers 22 moments of the solution when constructing the radial shape over each axial mesh of each assembly. For the axial variation, the node average and upper and lower surface fluxes are combined to produce a quadratic shape over each axial mesh. The fitting basis in the radial plane is far more complex than that of DIF3D-FD shown earlier. The RCT fitting allows for a complete fourth order x-y polynomial expansion (15 monomials) in addition to 7 additional higher order terms that are up to 7th order.

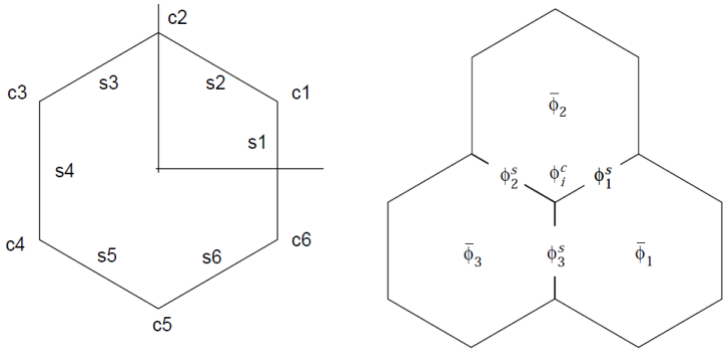

Figure 6-3. Basic components of the DIF3D-Nodal radial fitting algorithm

What should be apparent from this fitting procedure is that the fitting technique being applied in adjacent assemblies is not congruent and can yield a result with discontinuities in the flux. Sub-division of the hexagonal mesh is not possible with DIF3D-Nodal or DIF3D-VARIANT. Refinements of the spatial basis or the mesh itself will likely not fully resolve those underlying discontinuities in the flux distribution in the domain. This is of course a minor concern for a pin power application as the compositional differences between adjacent regions tend to impose discontinuities regardless of the flux or fitting discontinuities. The RCT approach to defining pin powers and pin densities given either the DIF3D-Nodal or DIF3D-VARIANT solution has been shown to be quite accurate and works primarily because of the underlying normalization that imposes it to preserve the mesh averaged reaction rate.

6.1.3 DIF3D-VARIANT Methodology for DASSH

The final aspect of pin power reconstruction to discuss is the approach used in DASSH. DIF3D-VARIANT makes a full 3D basis expansion of the flux written simply as:

$$\psi_g(x,y,z,\Omega) = \sum_{i,j} f_i(x,y,z) * g_j(\Omega) * \bar{\psi}_{g,i,j} \tag{6.1}$$

DIF3D-VARIANT obtains the coefficients of the expansion, $\bar{\psi}_{g,i,j}$, during the iterative solve of the steady state eigenvalue or fixed source problem and stores them in the NHFLUX file. Because reaction rate distributions do not require the angular flux moments, DIF3D will only store the diffusive moments in the file NHFLX0 which can save considerable disk storage cost and improves the performance. The scalar flux stored in this file can be represented as:

$$\phi_g(x,y,z) = \sum_i f_i(x,y,z) \cdot \bar{\phi}_{g,i} \rightarrow \bar{f}^T \bar{\phi}_g \tag{6.2}$$

The spatial flux $f_i(x,y,z)$ is a complete Nth order orthogonal polynomial expansion within each mesh but the z direction basis can be truncated to a lower Lth order expansion via the DIF3D input.

For hexagonal-Z geometries appropriate for ABR-1000, each hexagon counts as one mesh in the radial plane and there are typically 20-40 axial meshes in any given DIF3D-VARIANT problem. The ABR-1000 study problem has 50 axial meshes and 397 hexagons for a full core model. The orthogonal polynomial set can be redefined in terms of a set of monomials as:

$$f_i(x,y,z) = \sum_k a_k(x,y,z) \cdot m_{i,k} \rightarrow \bar{f} = \bar{\bar{M}}\bar{a} \tag{6.3}$$

In the monomial form, it is a trivial matter to evaluate the polynomial basis which starts by evaluating the coordinate direction monomials first, e.g. $1, x, x^2, x^3, \ldots, x^N$, at the point of interest. Note that this requires a linear transformation from the real space into the reference space of each mesh. The coordinate direction monomials are combined to produce the full set of monomials $a_k(x,y,z)$ and thus the monomial vector space $\bar{a}$ at the point of interest. The $\bar{\bar{M}}$ matrix multiplication is provided by DIF3D-VARIANT and used to construct the polynomial functions from the monomials ones and thus collapsed by the set of coefficients from NHFLX0 to get the point evaluation of the flux at (x,y,z).

$$\phi_g(x,y,z) = \bar{m}^T \bar{\bar{M}}^T \bar{\phi}_g \tag{6.4}$$

The primary difference between the DIF3D-VARIANT and other solvers in DIF3D is the ability to fully capture the 3D power distribution with a simple to evaluate monomial expression. The expression in equation 4 can be evaluated at any point within a given mesh such as pin locations, duct wall, and even coolant sub-channels. For DASSH, the flux shape within each DIF3D mesh is evaluated at the center of each pin (as opposed to an integral over a circle) and the axial integral is analytic within each mesh. This is a valid methodology as the flux gradients over any given pin are not considerable in a fast reactor.

To understand whether this aspect is important, Figure 6-4 provides normalized plots of the pin power distribution for the center pin and six corner pins of the third assembly in ring 8 of the ABR-1000 problem (circled assembly in the inset picture). The axial discontinuities are caused by a combination of the compositional differences between axial meshes and the mesh-wise power normalization.

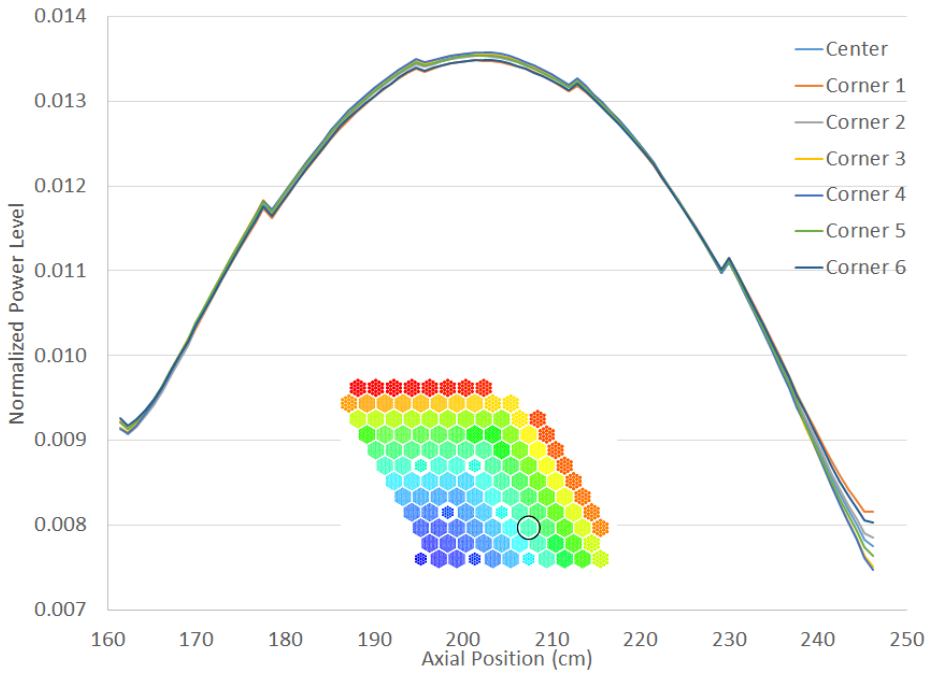

Figure 6-4. Radial variation in the axial distribution for assembly 3 in ring 8 of ABR-1000

The normalization ensures the differences in the radial magnitude are of no consequence and one can see that there are rather minor differences in the axial power shape for this assembly (generally less than 1% difference with a peak of ~10% at the upper end). In the SE2ANL and RCT methodologies, the radial distribution was assumed to be constant and independent of the axial distribution and Figure 6-4 clearly shows that this assumption will work quite well. Some cases where this assumption may not hold include problems with partially inserted control rods and the extreme case of a partially inserted fueled control rod. ABR-1000 does not have these features and thus those impacts are not shown here for brevity.

6.2 Power Decomposition for an Assembly

The last aspect to discuss is how the power is distributed within an assembly. Fundamentally heating of the fuel, cladding, and coolant occurs due to interaction of all material components with the neutron and gamma flux. The transport of the gamma flux from its generation point (typically fission in the fuel rods) to its absorption point in the domain is of significant importance for thermal hydraulics in a sodium cooled fast reactor. GAMSOR was specifically built to facilitate the coupled neutron-gamma transport calculation to obtain proper power generation in the non-fuel assemblies. In GAMSOR, the DIF3D code is used to solve the neutron transport problem. Given the neutron flux solution, the gamma emission source from neutron interactions is constructed and DIF3D is then ran again to obtain the gamma flux. The heating cross sections were evaluated by MC^2-3 and used by the GAMSOR output to produce the power distribution in the domain.

The application purpose of SE2ANL and DASSH are identical while RCT is somewhat different. For SE2ANL and DASSH, it should come as no surprise that the power distribution is obtained from GAMSOR although DASSH can obtain a power distribution from a regular DIF3D setup. In SE2ANL, the power is allowed to be distributed in one of two ways within each assembly:

1. Both gamma and neutron heating emanate from the pellet section of the array of pins
2. Neutron heating emanates from the fuel pellet while all gamma heating emanates from the duct wall

Of the two options for SE2ANL assembly power distribution, the first option is almost always used while the second option generally has displayed a rather minor impact even if it is not physically realistic.

The DASSH methodology allows the user more options to distribute the power. First, the assembly neutron and gamma power are separated into fuel, structure, and coolant via an input directive from the user. The equation 4 power distribution is evaluated in each sub-channel discretization of a given assembly, an example of which is shown in Figure 6-5. In this example, the coolant sub-channels are indicated with red letters and are assumed to produce the neutron and gamma power from the coolant.

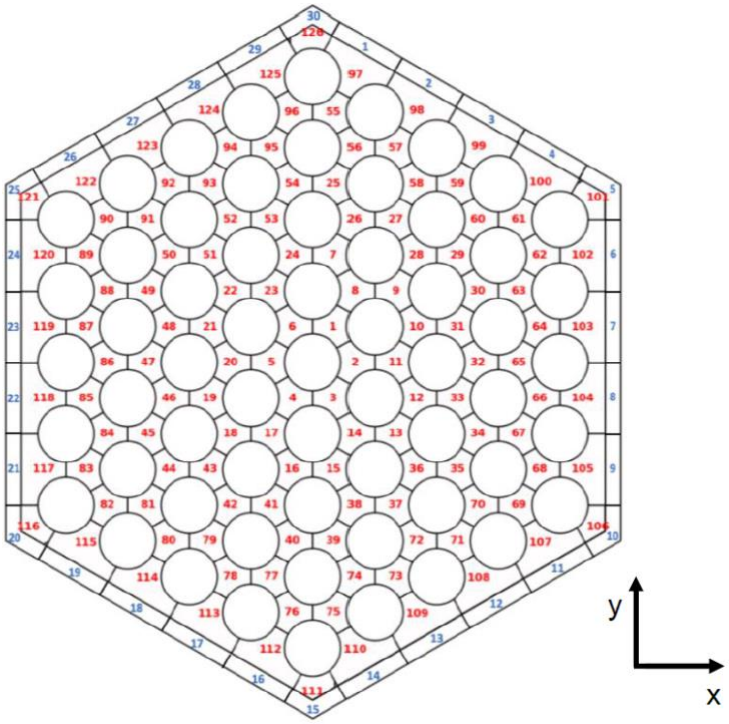

Figure 6-5. DASSH example sub-channel meshing of a 61 pin assembly

The array of pins (not numbered) produce all of the fuel neutron and gamma power along with the cladding and wire wrap fraction of the structure neutron and gamma power. Finally, the duct wall meshes (blue numbered sub-channels) take the remaining structure neutron and gamma power. This approach is the most rigorous one that can be used to define the power distribution in the assembly for the underlying thermal-hydraulics problem being solved in DASSH.

In DASSH, the distribution of neutron and gamma power has three options

1) The neutron and gamma power is split into fuel, structure, and coolant and assigned appropriately to the pin, duct, and coolant sub-channels

2) The neutron power emanates from the pins while the gamma heating emanates from the duct wall (i.e. SE2ANL approach)

3) The neutron and gamma power emanate from the pins

All three distributions are obtained by effectively evaluating equation 4 at each sub-channel centroid (pin center, duct wall mesh and coolant mesh). To make the computation independent of the axial meshing, an axial monomial basis, $1, z, z^2, z^3, \ldots, z^L$ is retained for each sub-channel mesh. This re-cast of the equation 4 setup is easy to do given the flux moments are expressed in terms of the monomials or $\bar{\varphi}_g = \bar{\bar{M}}^T \bar{\phi}_g$. With $\bar{\varphi}_g$, the order of the z term in the monomial is used to determine which vector position the evaluated x-y monomial terms are to be combined into. This produces a total (neutron + gamma) sub-channel power distribution of the form

$$\mathrm{P}_{i,k}(z) = \sum_{l=0}^{L} z^l \cdot p_{l,i,k} \tag{6.5}$$

where $p_{l,i}$ are the coefficients of the axial power expansion in the i[th] sub-channel of the assembly for a given DIF3D axial mesh *k*. The z monomials can be evaluated once for all assemblies for each axial thermal-hydraulics mesh as they are identical across all assemblies. It is easy to obtain an analytic integral of the axial expansion shown in equation 5. It is also easy to obtain a discrete integral using a midpoint integration rule, which is what the thermal-hydraulics axial mesh evaluation constitutes. Combining these, one can ensure that the power evaluation is always exactly preserved for any DASSH meshing so long as it preserves the originating DIF3D meshing.

As stated, RCT is somewhat different. In RCT, the development purpose was to model EBR-II pin depletion aspects and provide input for follow on fuels modeling codes. The former aspect is handled with the coupled solve of REBUS and RCT while the latter is handled with SE2RCT [21]. SE2RCT is Superenergy-2 coupled with RCT for the pin power distribution. SE2RCT is effectively identical to SE2ANL in purpose but solves a much smaller thermal-hydraulics problem: seven total assemblies where the central assembly has the targeted pin(s) for the follow-on fuels modeling code. In RCT and SE2RCT, the GAMSOR power distribution is not used but the conventional DIF3D one is. This tends to slightly over predict the power being deposited for EBR-II in addition to pushing all the power into the pins. The former issue of course leads to slightly higher coolant temperatures while the latter higher fuel temperatures, but this is of minor importance given the way RCT and SE2RCT are being used. In SE2RCT, all of the power is assigned to the pins which is identical to the first option of SE2ANL and last option of DASSH.

Regardless of whether SE2ANL, DASSH, or SE2RCT are being used, one key requirement is that the total power being produced in the pin, duct, and coolant must preserve the total power of each mesh. For SE2ANL, this is accomplished as described earlier by making the radial distribution a simple factor which sums to 1.0 across all pins. The neutron and gamma power is distributed evenly throughout the duct for a given axial mesh. For DASSH, the component power distribution is analytically integrated and the sum over all sub-channels is imposed to preserve the total power of the DIF3D mesh by component (fuel, structure, coolant). This approach in DASSH can cause axial discontinuities to appear which will be discussed later in this report. In SE2RCT, the fitting function and the pin evaluations are all imposed to exactly preserve the total power of the mesh.

6.3 EvaluateFlux Based Pin Power Methodology

EvaluateFlux is a utility program included in every distribution of DIF3D and its primary goal is to generate flux and reaction rate traverses through the domain. The motivation behind EvaluateFlux was to obtain foil reaction rates for experimental measurements taken in ZPR and ZPPR critical assemblies. Previous to EvaluateFlux, the foil evaluation was done using the mesh averaged flux available from the regular DIF3D output which was not reliable for off center foil locations.

From the earlier discussion on fast reactor pin power reconstruction, it should be quite apparent that EvaluateFlux can be used to obtain pin, duct, and coolant power distributions within an assembly. As was the case with the SE2ANL, DASSH, and SE2RCT methodologies, using EvaluateFlux to produce a power distribution requires a normalization be applied to preserve the total mesh power. Because EvaluateFlux was only written to provide the pointwise evaluation, the user must build their own normalization scheme around the EvaluateFlux output and this is not discussed here for brevity.

Similar to the routines in DASSH, EvaluateFlux uses equation 4 to evaluate the point-wise flux in every DIF3D mesh. The default usage of EvaluateFlux will generate the multi-group flux at each point (GEODST and NHFLUX files are provided). If the LABELS, NDXSRF, ZNATDN, and ISOTXS files are provided, the conventional reaction rates (fission, capture, n,alpha, power, etc…) for the composition assigned to each mesh point are provided. The power reaction rate distribution produced by EvaluateFlux is equivalent to that used by DIF3D and not that of GAMSOR. To make use of GAMSOR, the VARPOW utility program must be used to generate the NHFLUX input file for EvaluateFlux (GEODST and NHFLUX input approach). VARPOW takes the GAMSOR created neutron and gamma NHFLUX files and combines them with the heating cross sections (PMATRX) to produce the neutron and gamma power distributions within each DIF3D mesh. VARPOW stores these spatial distribution details in a NHFLUX formatted file which can be used by EvaluateFlux to obtain point-wise evaluations of the neutron and gamma power throughout the domain. VARPOW also has the ability to split the neutron and gamma power amongst fuel, coolant, and structure such that EvaluateFlux can also obtain a spatial distribution breakdown similar to what DASSH is doing.

6.4 ABR-1000 Pin Power Distribution Comparison Details

As part of the methodological review comparison, the assembly power distribution details should be compared between the ANL and TerraPower teams. In this section, the pin power results generated and provided by ANL are discussed. To begin, the full monomial power distribution for each assembly is exportable, but this was deemed too difficult for comparison purposes at this time. The axially integrated pin power is provided along with a 3D spatial discretization for the pin power distribution. Also covered in this section is a brief discussion of the impact of space-angle approximations on the pin power results and the changes in power associated with the component representation.

The DASSH methodology only provides pin power details on the part of the domain considered to be heterogeneous. For the ABR-1000 description, the geometry only specifies a heterogeneous geometry description above the lower structure to the top of the upper plenum. Thus, in DASSH, the pin power distributions only consider power derived from the geometry starting at 35.75 cm and ending at 367.81 cm in the ABR-1000 model. All power from meshes in

the lower structure up to 35.75 cm and the upper structure from 367.81 cm to 480.20 cm is not included in the pin power distributions shown here or provided as data files. That power is accounted for in DASSH via a porous body medium approximation of those parts of the domain which is beyond the scope of this document and it is noted that the power would be a rather minor change in the total power being used.

Because the third core symmetry (120 degree periodic) geometry gives the same power distribution details as the full core geometry, the data files provided by ANL for pin power are for the 120 degree periodic space. Figure 6-6 provides a visual example of the third core symmetry pin power distribution. As can be seen, the hexes on the periodic part of the domain are not duplicated and the central assembly appears as though it is outside of the regular geometry rather than at the center. It is important to note that while the neutronics specified power distribution does not change, the thermal-hydraulics calculation of a full core versus a third core symmetry model are slightly different. This is because the thermal-hydraulics problem does not really have the stated symmetry because of the swirling coolant within each assembly and the third core symmetry thermal hydraulics problem is thus in error with respect to a full core model.

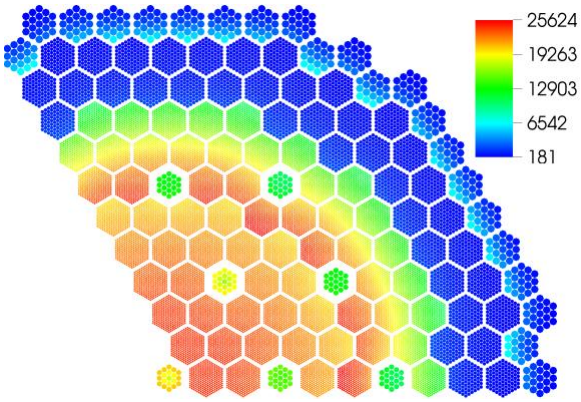

Figure 6-6. Axially integrated pin power (watts) distribution for 120 degree periodic ABR-1000

Figure 6-7 graphically displays the impact of defining the pin power distribution over just the active core versus the specified pin lattice geometry in ABR-1000. All of the power in each assembly is deposited in the pins (no duct or coolant heating). As can be seen, the peak pin power only goes up slightly (25,372 watts to 25,624 watts) and most of the driver pin power details appear nearly identical.

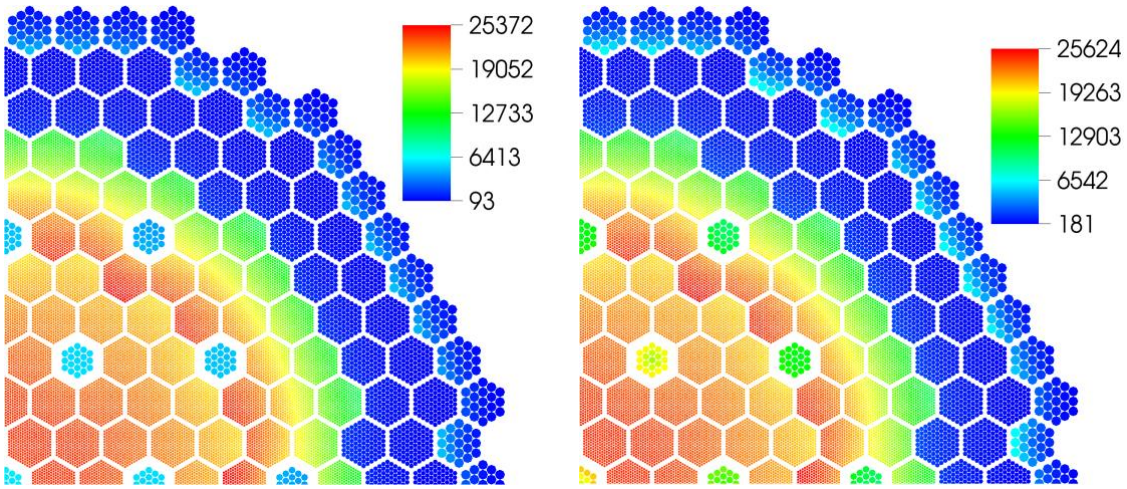

160.92 to 246.74 cm (Active Core) 35.75 to 366.81 cm (Full Heterogeneous)

Figure 6-7. Axially integrated pin power (watts) for active core versus modeled geometry

In reality, all of the driver pins go up slightly, rather similarly to the peak pin power, because of the additional axial volume added to the power integral. The areas of greatest change in the two pictures of Figure 6-7 are the control rods. In the ABR-1000 model, the control rods are parked just above the active core and thus when they are excluded, the power deposited into the control material is not included. One should also then understand that the power that is present in the active core and lower reflector (typically an empty hex can) is not actually deposited in the pin geometry as seen, but in the coolant and duct wall. In this regard, the control rod pin power result is the most convoluted aspect of the pin power results provided by ANL. While DASSH can allow the power to be distributed by material, for the purposes of the comparison, assuming that the power is located in the pins is acceptable.

DIF3D-VARIANT allows the user the ability to apply diffusion theory, P_N transport theory, and SP_N transport theory. In this regard, it is worth discussing and displaying how these various power distributions differ on the ABR-1000 problem. Table 6-1 provides the ABR-1000 k_{eff} results when using a 6^{th} order flux and source approximation combined with a 1^{st} order leakage approximation and different angular methodologies. These k_{eff} results differ from the reference results provided in section 3.1.2 due to the less rigorous approach used to generate the multi-group cross sections in MC^2-3 for gamma heating calculations (1-step without 1D treatment).

Table 6-1. k_{eff} results for ABR-1000

Methodology	k_{eff}
Diffusion	1.00149
P_3P_3	1.00703
SP_3P_0	1.00654
SP_3P_1	1.00368
SP_3P_3	1.00431

As can be seen, diffusion is about 600 pcm below the P_3P_3 transport result. The SP_3P_0 case yields an eigenvalue result that is very similar to P_3P_3 while the SP_3P_1 result is about 340 pcm below and the SP_3P_3 result is 270 pcm. In this particular case, one could conclude that the conventional way to use SP_N (with isotropic scattering) will yield a result similar to the transport result with a fraction of the computational cost. However, one should check the other reaction rates before definitively assuming that, which is done here for just the pin power.

Figure 6-8 shows the difference in the spatial distribution of pin powers across the entire core when using diffusion theory versus transport. As seen, the spatial distribution appears identical, however one can see that the P_3P_3 solution has a slightly higher peak pin power compared with the diffusion theory result. From this comparison, it should be clear that a whole core perspective is insufficient to actually display the impact of using transport and thus individual assemblies are displayed for more clarity.

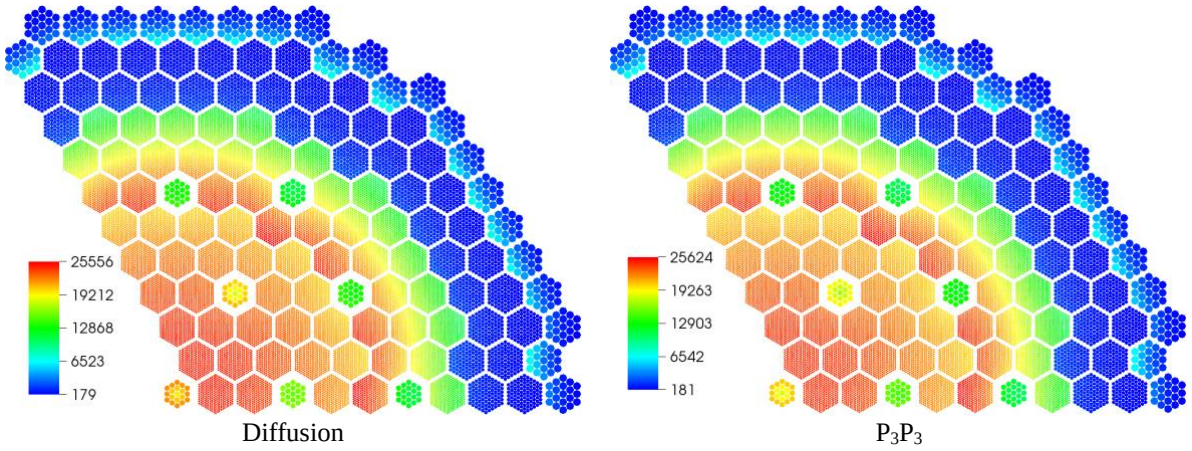

Diffusion P_3P_3

Figure 6-8. Axially integrated pin power (watts) for diffusion versus P_3P_3

Figure 6-9 shows the five selected assemblies in the reactor model that will be used for the pin power comparisons. These assemblies were chosen because of their gradients or importance in the calculation noting that at least one of each assembly type is displayed.

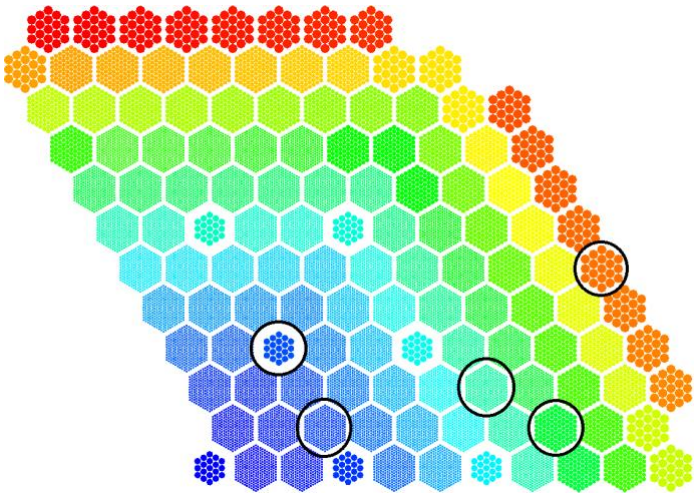

Figure 6-9. Selected assemblies (circled) for the pin level comparisons

Starting with the driver assembly in position 2 of ring 4, it was chosen for a detailed comparison as it is adjacent to a control assembly. Figure 6-10 provides the pin power distributions for four of the five angular approximations in Table 6-1. For the peak pin in this assembly, the four cases shown have 24051, 23785, 23783, 23833 watts for the peak pin, respectively. This constitutes less than a 1% difference between the diffusion and transport results where the SP_N results are less than 0.2% different from the transport results.

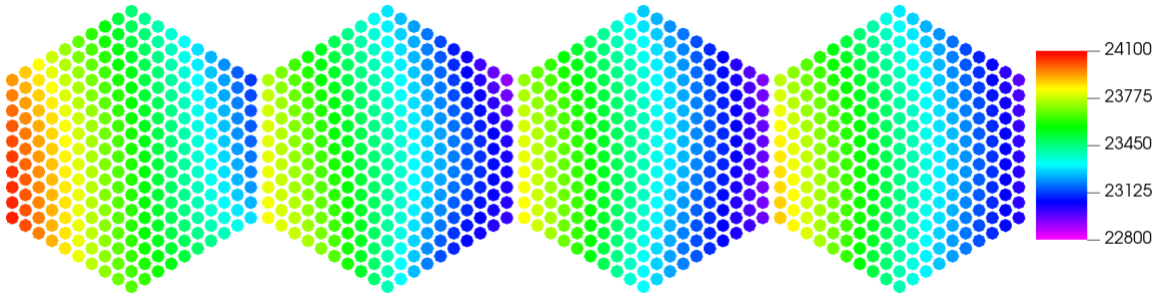

Diffusion P_3P_1 SP_3P_0 SP_3P_1

Figure 6-10. Pin power (watts) comparison for the driver assembly in position 2 of ring 4

Continuing, Figure 6-11 provides the comparison for the driver assembly in position 3 of ring 8. This assembly was chosen because of the steep power gradient which is observable in Figure 6-8. Unlike Figure 6-10, the pin power distributions all look very similar in Figure 6-11. The peak pin power in these four plots is 21732, 21905, 21928, and 21848 watts, respectively. As was the case in the previous assembly, the diffusion theory result is less than 1% in error with the P_3P_3 case and the SP_N cases are less than 0.3% in error.

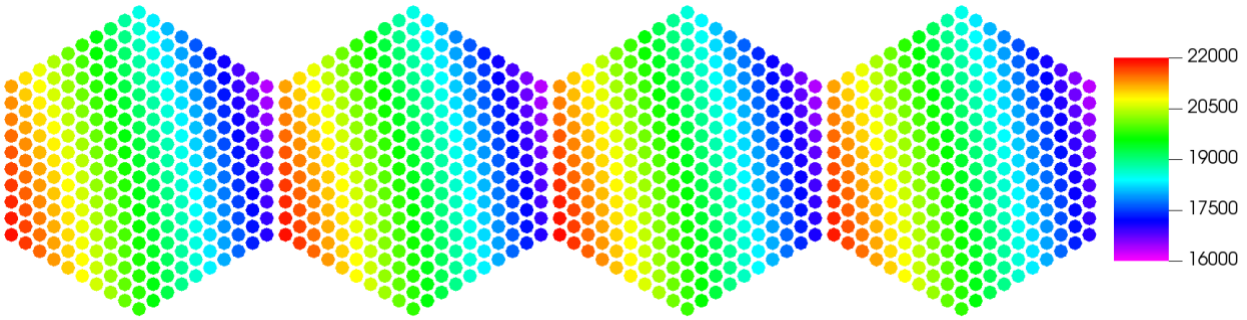

Diffusion P_3P_1 SP_3P_0 SP_3P_1

Figure 6-11. Pin power (watts) comparison for the driver assembly in position 3 of ring 8

The next assembly considered is a reflector assembly in position 2 of ring 9 the pin power plot of which is provided in Figure 6-12. There are more visible differences between the diffusion and transport solutions in Figure 6-12 along with the SP_N and transport solution. The peak pin power results in this assembly are 2285, 2161, 2225, and 2211 watts, respectively. In this case the

diffusion to transport error is ~6% while the SP_N errors are 2-3%. These are notably larger errors from those observed in the driver assemblies.

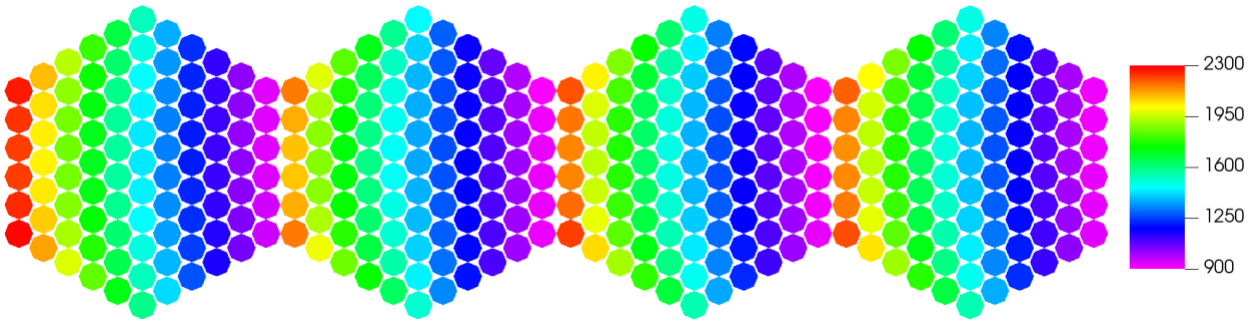

Diffusion P_3P_1 SP_3P_0 SP_3P_1

Figure 6-12. Pin power (watts) comparison for the reflector assembly in position 2 of ring 9

The next assembly to be considered is the shielding assembly in position 6 of ring 12 which is plotted in Figure 6-13. The differences between the diffusion and transport approximation is again clear while the differences between the transport and SP_N results are difficult to discern. The peak pin power in each assembly is 7088, 6683, 6829, and 6859 watts, respectively. The diffusion result is 6% above the P_3 transport results while the SP_N results are 2-3% in error with the P_3 result, similar to the preceding reflector assembly.

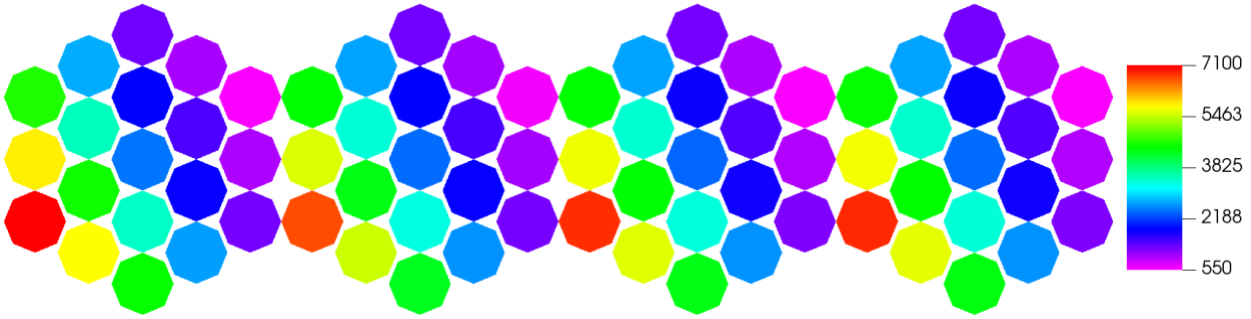

Diffusion P_3P_1 SP_3P_0 SP_3P_1

Figure 6-13. Pin power (watts) comparison for the shield assembly in position 6 of ring 12

The last assembly to consider is a control assembly from position 4 of ring 4 shown in Figure 6-14. Once again, there are notable differences between the diffusion and transport results and the SP_N results are also notably different from the transport one. The peak pin power for this assembly for the four cases is 20704, 19397, 19796, and 19863 watts, respectively. This shows a ~7% error between the diffusion and transport result and 2-3% errors for the SP_N to the transport result. The control assembly is rather unique in that most of the power is coming from the axial regions directly above the active core. In this regard, it is just as sensitive to the leakage from the reactor as the reflector assemblies are and clearly the diffusion theory result has a consistently higher power distribution.

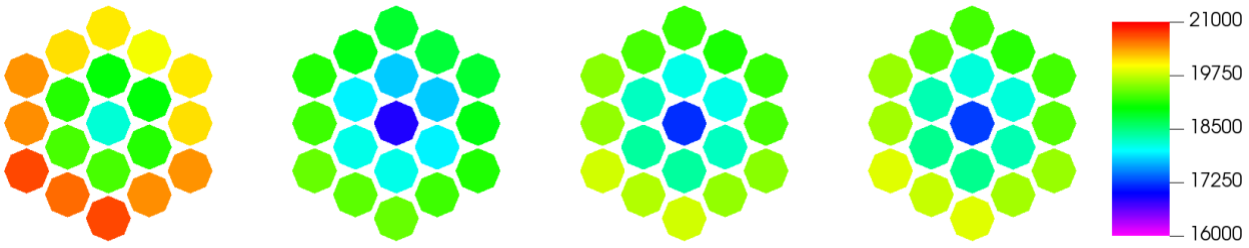

Diffusion P_3P_1 SP_3P_0 SP_3P_1

Figure 6-14. Pin power (watts) comparison for the control assembly in position 4 of ring 4

For the sake of completeness, the impact of GAMSOR on the pin power distribution can be displayed. Figure 6-15 shows the pin power distribution details for GAMSOR and those from DIF3D where the total domain power was normalized to be exactly the same. For the most part the DIF3D results for the driver assemblies are rather similar which is expected as the bulk of the power is derived from the fuel itself. However, the radial reflector assemblies have rather high differences of ~20%. The shielding assemblies are more similar than the reflector assemblies with <10% errors as Figure 6-15 would imply. Lastly, the control assemblies are remarkably different with >30% errors which is also obvious in Figure 6-15. Because GAMSOR relies upon the transmission of gamma rays and uses the heating cross sections, the displayed differences are entirely due to these features of GAMSOR thereby justifying using it over the DIF3D approach.

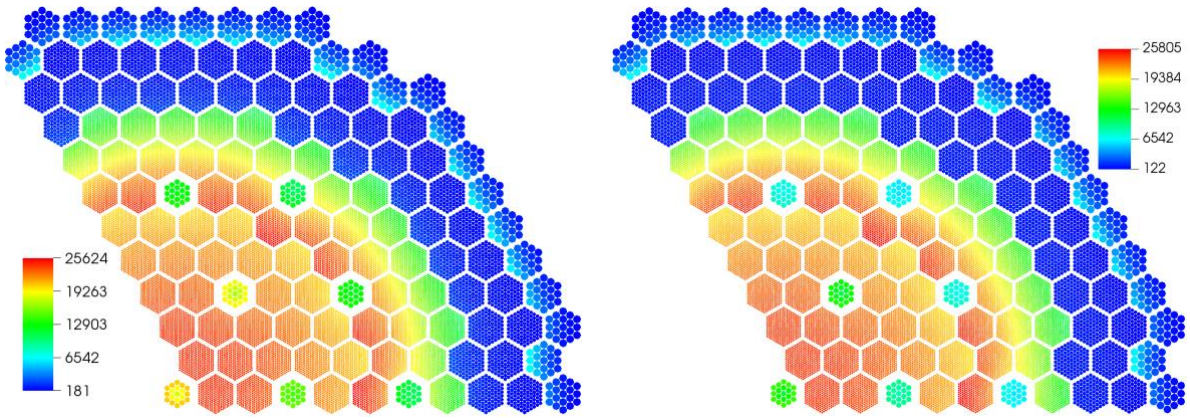

GAMSOR DIF3D

Figure 6-15. Axially integrated pin power (watts) for GAMSOR versus DIF3D

All of the preceding results are focused on axially integrated pin power. While they are sufficient to display differences between the diffusion and transport result, there is an axial aspect of the power distribution that is important to consider. Consequently, the axial profile of the center pin of the driver assembly in position 2 of ring 4 is plotted in Figure 6-16. Figure 6-17 similarly provides the peak pin power of the control assembly in position 4 of ring 4 (see Figure 6-14), while Figure 6-18 provides the peak pin power of the shield assembly in position 6 of ring 12 (see Figure 6-13).

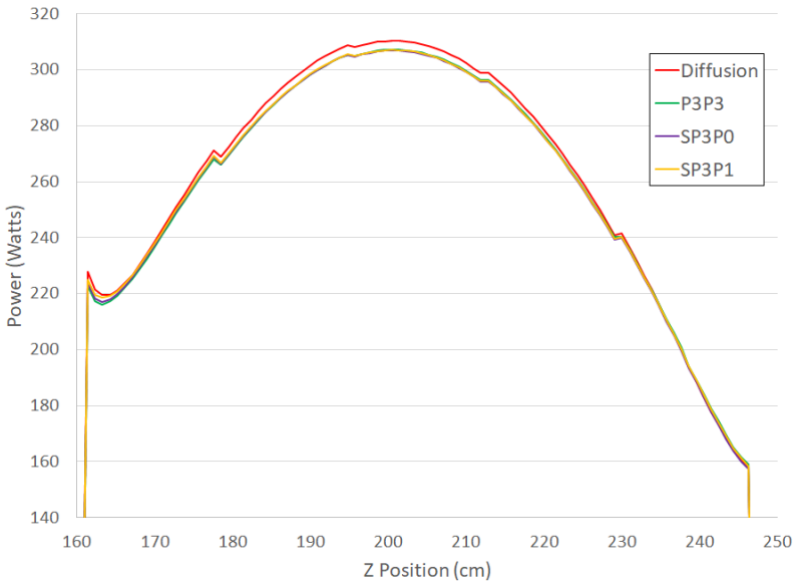

Figure 6-16. Axial pin power (watts) traverse for pin 1 of assembly 2 in ring 4

Starting with the driver assembly in Figure 6-16, one can clearly see that the diffusion result is noticeably different from the P_3P_3 transport result. The two SP_N solutions however are nearly indistinguishable from the transport result. For the control assembly in Figure 6-17, one can see that the power in the active core region is ~6 times lower than the peak power that occurs at the tip of the control rod just above the active core. There is a much smaller peak that appears below the core because of a change in the sodium volume fraction of this assembly position at this position. Overall, the diffusion theory result is difficult to distinguish from the transport and SP_N but there are visible differences.

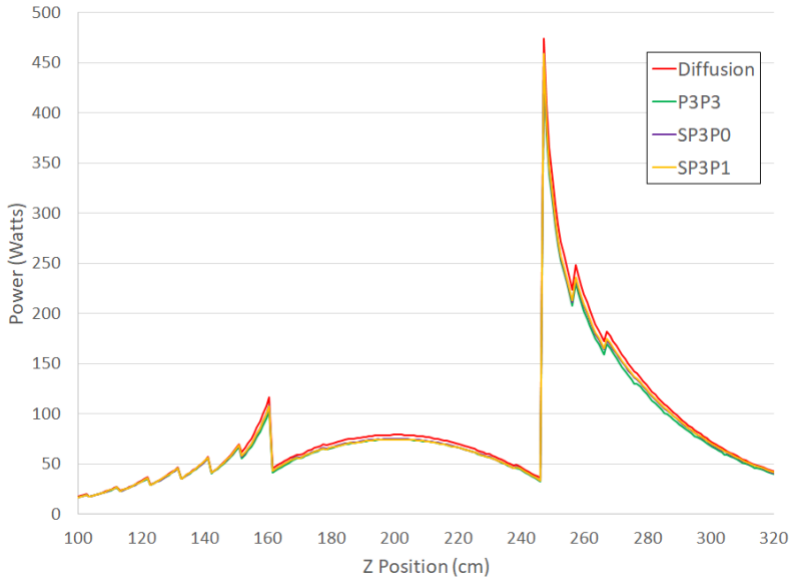

Figure 6-17. Axial pin power (watts) traverse for high power pin of assembly 4 in ring 4

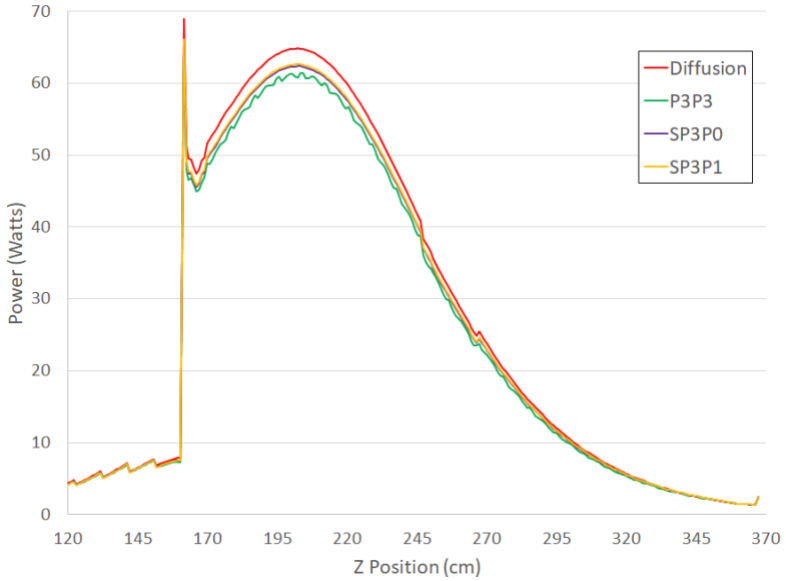

Figure 6-18. Axial pin power (watts) traverse for high power pin of assembly 6 in ring 12

The shield assembly result in Figure 6-18 likely has the greatest differences. The wiggles in the P_3P_3 solution are due to a lack of iterative convergence. The iterative algorithm of DIF3D-VARIANT focuses on the flat moments of the flux and the higher order moments are typically less converged. The diffusion and SP_N theory approaches do not suffer the same fate because they are better conditioned systems. While one could increase the convergence on the transport solution, it was not done in this work as the general shape of the power profile is sufficient for the needs of this comparison. From Figure 6-18 one can easily identify differences between the diffusion and P_3P_3 curves. The reason for the lower peak is not entirely clear at this time but there is a significant material change that occurs at that axial height as the B-10 section does not extend to the bottom of the domain. Because the power shape is a result of the flux profiles, the most likely explanation is that the flux profiles change radically near this boundary due to improved thermalization in the lower, non-boronated region below the B-10 section. If that is the case, then the cross sections being used are likely not valid as the energy-group structure used in MC^2-3 is not reliable in the thermal range.

In all of the axial plots in Figure 6-16 to Figure 6-18, there are observable discontinuities in the solution which correspond to the boundary of axial meshes. In the driver assemblies, the discontinuities displayed are primarily because of the 5 axial compositions used in each fuel assembly in the depletion model. This approach causes a base difference in the actinide concentrations (U-235 and U-238) which imposes a discontinuity in the power even if the flux solution is not discontinuous at the boundary.

In the control rod assembly, there are both compositional discontinuities and power normalization induced discontinuities present. Near the control rod tip and the bottom of the active core are the largest discontinuities which are due to the composition changes. The remaining discontinuities are caused by the power normalization scheme itself. To understand this, a simple 2 pin normalization assumption is shown in Figure 6-19. In this case, two pins in the control rod are selected and EvaluateFlux is used to obtain the axial distribution near the mesh interface. As

can be seen, the flux solutions for both pin locations are smooth as it transitions across the mesh interface (as expected). If all of the power is imposed to come from just these two pins in the assembly, that causes the power shape of each pin to change not only its magnitude, but also its slope (the numerator of the slope is altered by the scaling factor but the denominator is not as it is the axial mesh height). Because the two axial meshes have different power levels, this causes the zig-zag pattern seen in those parts of the reactor where no apparent composition changes are occurring.

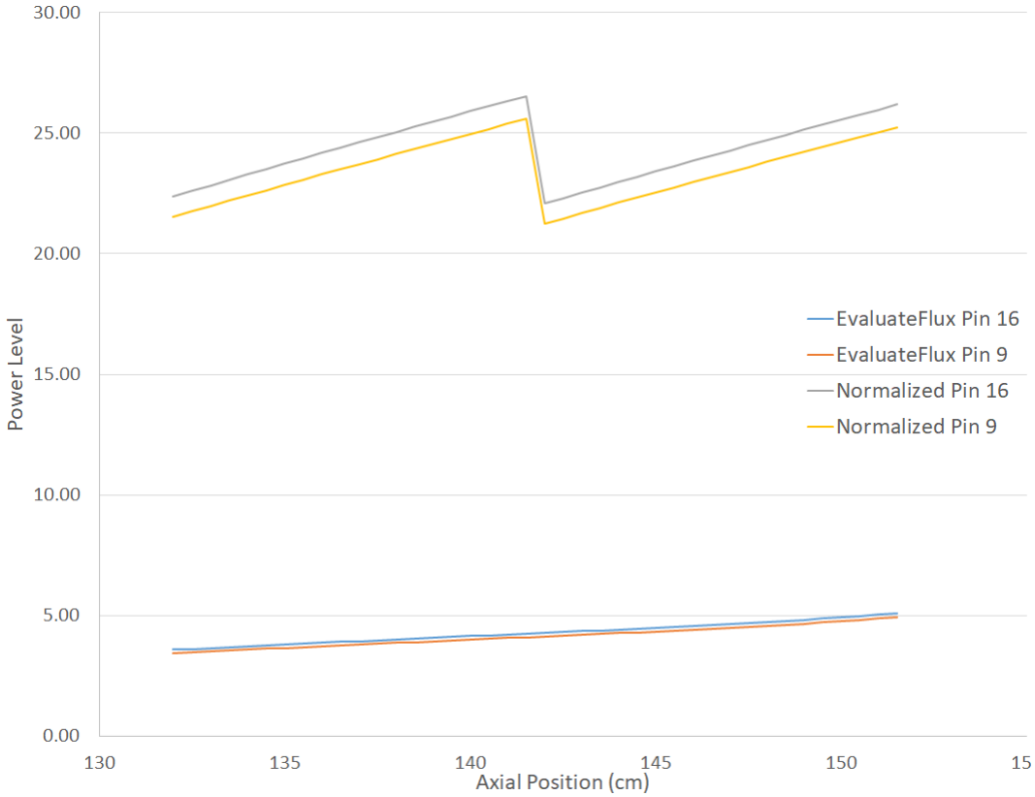

Figure 6-19. Power normalization induced discontinuities

As the number of fuel pins increases, the magnitude of these discontinuities will reduce. An alternative approach to the mesh-wise power normalization would be to normalize the power shape of all axial meshes in an assembly by the sum of the power in all of the axial meshes. This would retain a smooth power shape over all of the axial meshes, excluding composition change induced discontinuities, but it would result in power being shifted axially in the domain which might have greater implications on the peak fuel and clad temperatures. Given the magnitude of the power discontinuities are small, the mesh-wise power normalization is still considered to be the best approach.

The last aspect to discuss are the differences between EvaluateFlux and the preceding results and the impact of different spatial approximations and the use of power distributions other than pin-only. Figure 6-20 provides the DASSH center pin power distribution from assembly 3 of ring 8 and includes the diffusion and P_3P_3 transport results identically setup to those in the preceding figures (pin only). It also includes the impact of assigning power to the coolant and duct wall

(termed Split). As can be seen, the diffusion curve trends below the P_3P_3 transport result over some of the axial domain. Using the Split approach also drops the power level from the pin only scheme, as expected, which amounts to ~1% at the core midplane.

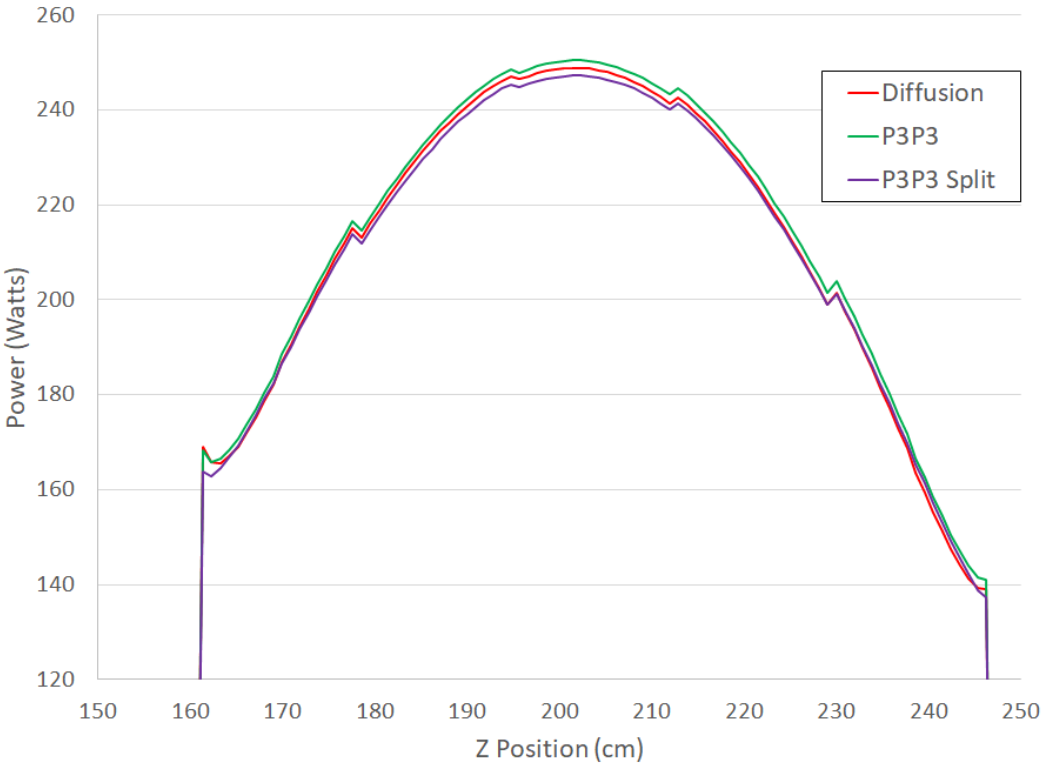

Figure 6-20. Axial pin power (watts) traverse in assembly 3 in ring 8

Figure 6-21 provides the EvaluateFlux result for the same pin in the same assembly. Because no volume is associated with the EvaluateFlux result, the units are watts/cm^3 and they cannot be directly compared against the results of Figure 6-20. While the two curves appear similar there are notable differences such as the magnitude of the variance across the axial domain and the large peak visible at the lower part of the core in EvaluateFlux. Both are related to the same artifact which is the volume being assigned to the plotted data in Figure 6-20 where no volume is assigned in Figure 6-21. At the lower end of the core, the peak is not as large in Figure 6-20 because the result is averaged over a given axial height. Further, the EvaluateFlux result also has more evaluation points (~0.5 cm spacing) while the DASSH approach in Figure 6-20 uses ~1 cm meshing where the very first is ~0.5 cm above the interface while EvaluateFlux displays a value nearly on the surface of the two meshes. The averaging aspect over the axial domain tends to reduce the appearance of the gradient in the two curves in addition to the normalization constraint applied to all of the pins in Figure 6-20. Also included in Figure 6-21 is the impact of switching from a 6th order spatial flux and source approximation to an 8th order. This was done with both, but EvaluateFlux shows the impact more clearly which is near negligible changes between a 6th and 8th order flux and source approximation. This is of course no surprise as the curves seen have at most a 4th order shape.

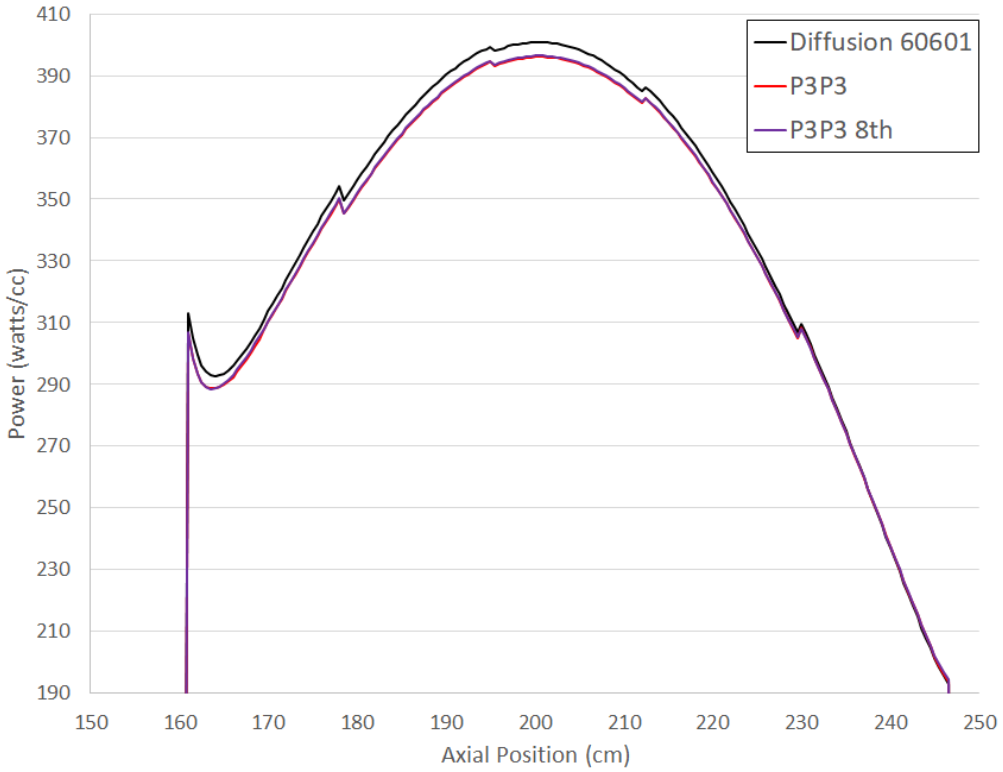

Figure 6-21. EvaluateFlux axial pin power (watts/cc) traverse in assembly 3 in ring 8

6.5 Pin Power Data File Descriptions

With the above displayed results, the collaborative work should focus on just a single result. For this, the pin only power with P_3P_3 transport was chosen. As stated previously, three files are provided which are listed, with descriptions, in Table 6-2. The excerpts for each file are provided in Figure 6-22, Figure 6-23, and Figure 6-24 as defined in Table 6-2. As stated earlier, all three files are based upon all of the power in each axial mesh from 35.76 cm to 367.81 cm being deposited in the pin lattice. The excerpts shown here might not identically match the ones that are provided as the work is ongoing and the review process might identify issues and thus these are just examples of the data being provided.

Starting with Figure 6-22, the axially integrated pin power, the excerpt has a header to separate each assembly. The time point details in the header are present because for a multi-time point calculation (beginning of cycle, middle of cycle, end of cycle, etc…) the output file would include the results for all time points. For the purposes of the present comparison, there is only one time point and thus this aspect of the output file can be ignored. The assembly number refers to the active node ordering specified by DIF3D-Nodal or DIF3D-VARIANT (they are the same). To make this more usable, the ring and position translation of each active node is provided along with the total power from the assembly which should match the sum of the pin powers being provided in this output file.

Table 6-2. Pin power comparison files

Name	Figure	Purpose
pinpower_3D_120_pinonly_P3P3.out	Figure 6-22	3D pin power details for each pin of each assembly targeting a 1 cm axial mesh height within each DIF3D mesh
pinpower_120_pinonly_P3P3.out	Figure 6-23	Axially integrated (35.76 to 367.81 cm) pin power details for each pin of each assembly
pinpower_mono_120_pinonly_P3P3.out	Figure 6-24	3D pin power details for the monomial distribution of each pin in each assembly for each DIF3D mesh

The second header line specifies what each column is in the pin power output detail. The first column of that output is "ID" which refers to the pin number. This number is provided for convenience of any discussion on pin power differences. More important are the second and third columns which give the X and Y coordinate center of each pin relative to the assembly position (i.e. not the global x-y coordinate). With this, the pin power result comparison should be easier to orchestrate regardless of how one choses to order the pins. The last column is of course the pin power in watts for each pin.

As can be seen from the remainder of the excerpt, this data layout repeats for each assembly in the active node ordering which happens to follow the ring and position ordering. Because this is for the 120 degree periodic space, only those assemblies appearing in Figure 6-6 will have pin power details shown here. While the NHFLUX and RTFLUX files do contain data for the hexes on the 120 degree periodic line, the results there are just a copy of the 0 degree line results and thus a rotation would have to be performed to extract a valid pin power distribution. Finally, it is important note that the central assembly contains a power level consistent with the full core and not the $1/6^{th}$ value that would be used in a power integral over the whole domain for a 120 periodic geometry.

Continuing with Figure 6-23, the 3D pin power excerpt, one can see that the output format is rather different from the previous one. While the assembly, ring, position header line remains effectively identical, the column layout is considerably different. The basic idea behind this output is to provide a pin power distribution that would normally be used in a thermal analysis of the system. The axial mesh attempts to use a ~1 cm mesh height and the result given is thus intended to be the integral over that ~1 cm mesh. In reality, what is provided is just the monomial shape function evaluated at the centroid of each mesh multiplied by the axial height of each mesh (~1 cm). Without a normalization this result will not lead to the exact axial pin power evaluation which will be discussed shortly.

The second and third header lines provide the X-Y coordinates of each pin while the third header line indicates that the first three columns are followed by pin numbering for each power result. As was the case for the axially integrated power, the X-Y coordinates should be used to match the pin powers in any comparison process. For each row of data, an index is provided for

each ~1 cm axial mesh that was created in each DIF3D mesh. In this example, the first DIF3D mesh extends from 35.76 cm to 45.38769 cm which was split into 10 meshes of height 0.96277 cm. For each axial mesh, the axial limits of the mesh are provided in columns 2 and 3. The pin power integral result for each axial mesh for each pin in the assembly are provided in the remaining columns.

In the DASSH scheme, the power integral of all pins for a given mesh is normalized such that the scheme being used will exactly match the power delivered by the DIF3D mesh. That was not done in this example and the resulting pin power distribution will thus have some discretization error. From the excerpt, after the very last axial mesh (366.8569 cm to 367.81 cm) one finds two measures of the pin power sum. The first is the simple sum, termed 'preceding", of the pin power was calculated using the unnormalized scheme discussed here. The second sum, termed "desired" is the result of analytically integrating the pin power monomial shape in each DIF3D mesh and summing over all DIF3D meshes. As can be seen in the first assembly, the error in the ~1 cm meshing is non-trivial and thus the importance of imposing an integral constraint is displayed. In a real thermal analysis, a 1 cm axial meshing is likely insufficient and thus the error will be reduced as the axial mesh size is decreased. Applying the provided desired pin power as a normalization scheme should be sufficient for the comparison work, but it is not consistent with what DASSH does and will lead to a slight disagreement with what ANL actually uses.

As was the case with the axially integrated pin power file, the 3D pin power file repeats the same information for each assembly in the domain. As was stated, the power was imposed to appear in the pin lattice even though for the empty control rod positions this does not make physical sense. Because the number of pins in the ABR-1000 extends well past the displayed column (271 pins versus the first 6 displayed here as an example). This file is quite large having 44960 lines of output and taking nearly 100 MB of disk space.

The excerpt in Figure 6-24 is from the last file which gives the pin power monomial distribution in each assembly. Again, the assembly header line appears before each section of assembly data. Unlike the previous outputs, this output file is a dump of the data structure internal to the code and thus additional details about the assembly are provided such as number of fuel pins, ducts, monomials, etc… Other than the number of explicit meshes - how many DIF3D meshes are used between 35.76 cm and 367.81 cm - these values can be ignored for the comparison. The number of DIF3D meshes is important as any comparison will require knowledge about the axial meshing in the DIF3D calculation which is provided here from the preceding 3D pin power distribution file.

In Figure 6-24, there are two sets of data for each assembly. The first set of data is the power sum that is used in the normalization process discussed for the 3D meshing approximation above. Since there are 35 axial DIF3D meshes, there are 35 values. The intention is that the sum of the pin powers for each DIF3D axial mesh should exactly yield this power. Given this information is provided in this file, one can apply the exact normalization used in DASSH to the results provided in the 3D pin power file Figure 6-23.

The second set of data in Figure 6-24 is the monomial distribution for each pin. Two header lines appear before the section of output data indicating what the columns are. The first column indicates which axial DIF3D mesh the data originates from. The second column indicates the pin ID which was provided in the previous two files with X-Y coordinates. Since the X-Y detail is not

stored in this data structure, it is not displayed in this output file, but it is a trivial matter to cross map the result shown here with either the first or second data files as they use the same fuel pin ID numbering. The remaining columns are of course the axial monomial expansion for each pin. In this excerpt, data for 7 monomials is provided corresponding to 1, z, z^2, z^3, z^4, z^5, and z^6 where the user input to DIF3D dictates what order this monomial basis will be.

As was the case with the preceding two data files, the third data file also repeats the same output detail for every assembly. With this last file, all of the necessary information is provided to exactly reproduce the pin power methodology actually being used by ANL for the power distribution in DASSH. While details on the duct wall and coolant power distribution are not studied as part of this comparison, it should be clear from the preceding displayed driver pin power results that these are a minor component to the total power in those assemblies and they can be ignored.

```
# Time point   1 pin powers (watts) for assembly      1 ring  1 position    1
with total power  3.794367E+05 watts.
# ID         X             Y       Pin Power (watts)
   1   5.329071E-15  0.000000E+00  1.814041E+04
   2   2.128690E+00  1.229000E+00  1.922564E+04
   3   5.329071E-15  2.458000E+00  1.922564E+04
   4  -2.128690E+00  1.229000E+00  1.922564E+04
   5  -2.128690E+00 -1.229000E+00  1.922564E+04
   6   5.329071E-15 -2.458000E+00  1.922564E+04
   7   2.128690E+00 -1.229000E+00  1.922564E+04
…
  18   4.257381E+00 -2.458000E+00  2.045223E+04
  19   4.257381E+00  0.000000E+00  2.039452E+04
# Time point   1 pin powers (watts) for assembly      2 ring  2 position    1
with total power  6.621255E+06 watts.
# ID         X             Y       Pin Power (watts)
   1   1.065814E-14  0.000000E+00  2.444165E+04
   2   7.764784E-01  4.483000E-01  2.443904E+04
…
 266   6.988305E+00 -1.344900E+00  2.437542E+04
 267   6.988305E+00 -4.483000E-01  2.437417E+04
 268   6.988305E+00  4.483000E-01  2.437417E+04
 269   6.988305E+00  1.344900E+00  2.437542E+04
 270   6.988305E+00  2.241500E+00  2.437776E+04
 271   6.988305E+00  3.138100E+00  2.438089E+04
# Time point   1 pin powers (watts) for assembly      3 ring  2 position    2
with total power  6.617348E+06 watts.
# ID         X             Y       Pin Power (watts)
   1   1.065814E-14  0.000000E+00  2.442707E+04
   2   7.764784E-01  4.483000E-01  2.442236E+04
…
# Time point   1 pin powers (watts) for assembly    132 ring 12 position   21
with total power  2.112282E+04 watts.
# ID         X             Y       Pin Power (watts)
   1   7.105427E-15  0.000000E+00  9.391737E+02
   2   2.910105E+00  1.680150E+00  8.613838E+02
   3   7.105427E-15  3.360300E+00  5.487250E+02
   6   6.217249E-15 -3.360300E+00  1.662234E+03
   7   2.910105E+00 -1.680150E+00  1.618757E+03
   8   5.820210E+00  3.360300E+00  6.824411E+02
   9   2.910105E+00  5.040450E+00  4.323125E+02
…
```

Figure 6-22. Comparison file pinpower_120_pinonly_P3P3.out excerpt

```
# 3D pin power shape for all active assemblies in the domain
# Time point   1 pin powers (watts) for assembly      1 ring  1 position    1 with total
power  3.794367E+05 watts.
#                X                5.329071E-15  2.128690E+00  5.329071E-15 -2.128690E+00 -
2.128690E+00  5.329071E-15…
#                Y                0.000000E+00  1.229000E+00  2.458000E+00  1.229000E+00 -
1.229000E+00 -2.458000E+00…
#Index    Lower Z      Upper Z        1             2             3             4
5             6        …
    1  3.576000E+01  3.672277E+01  2.694036E-01  2.691309E-01  2.691309E-01  2.691309E-01
2.691309E-01  2.691309E-01…
    2  3.672277E+01  3.768554E+01  2.770529E-01  2.768084E-01  2.768084E-01  2.768084E-01
2.768084E-01  2.768084E-01…
    3  3.768554E+01  3.864831E+01  2.866886E-01  2.864920E-01  2.864920E-01  2.864920E-01
2.864920E-01  2.864920E-01…
…
    9  4.346215E+01  4.442492E+01  3.675351E-01  3.675828E-01  3.675828E-01  3.675828E-01
3.675828E-01  3.675828E-01…
   10  4.442492E+01  4.538769E+01  3.839071E-01  3.839350E-01  3.839350E-01  3.839350E-01
3.839350E-01  3.839350E-01…
    1  4.538769E+01  4.635046E+01  4.011655E-01  4.010781E-01  4.010781E-01  4.010781E-01
4.010781E-01  4.010781E-01…
…
   11  3.659039E+02  3.668569E+02  9.996253E-02  1.001274E-01  1.001274E-01  1.001274E-01
1.001274E-01  1.001274E-01…
   12  3.668569E+02  3.678100E+02  9.856948E-02  9.874283E-02  9.874283E-02  9.874283E-02
9.874283E-02  9.874283E-02…
#Pin power (watts) preceding       9.024028E+03  1.009245E+04  1.009245E+04  1.009245E+04
1.009245E+04  1.009245E+04…
#Pin power (watts) desired         9.145849E+03  1.013949E+04  1.013949E+04  1.013949E+04
1.013949E+04  1.013949E+04…
# Time point   1 pin powers (watts) for assembly      2 ring  2 position    1 with total
power  6.621255E+06 watts.
#                X                1.065814E-14  7.764784E-01  1.065814E-14 -7.764784E-01 -
7.764784E-01  1.065814E-14…
#                Y                0.000000E+00  4.483000E-01  8.966000E-01  4.483000E-01 -
4.483000E-01 -8.966000E-01…
#Index    Lower Z      Upper Z        1             2             3             4
5             6
    1  3.576000E+01  3.672277E+01  5.423457E-02  5.415898E-02  5.422677E-02  5.429457E-02
5.429457E-02  5.422677E-02…
    2  3.672277E+01  3.768554E+01  5.577617E-02  5.570000E-02  5.576929E-02  5.583858E-02
5.583858E-02  5.576929E-02…
    3  3.768554E+01  3.864831E+01  5.771765E-02  5.764068E-02  5.771218E-02  5.778369E-02
5.778369E-02  5.771218E-02…
…
# Time point   1 pin powers (watts) for assembly    132 ring 12 position   21 with total
power  2.112282E+04 watts.
#                X                7.105427E-15  2.910105E+00  7.105427E-15 -2.910105E+00 -
2.910105E+00  6.217249E-15…
#                Y                0.000000E+00  1.680150E+00  3.360300E+00  1.680150E+00 -
1.680150E+00 -3.360300E+00…
#Index    Lower Z      Upper Z        1             2             3             4
5             6
    1  3.576000E+01  3.672277E+01  3.729162E-02  3.425604E-02  2.416179E-02  2.481356E-02
3.684637E-02  5.251461E-02…
    2  3.672277E+01  3.768554E+01  3.759212E-02  3.457980E-02  2.399306E-02  2.463795E-02
3.724679E-02  5.331350E-02…
    3  3.768554E+01  3.864831E+01  3.833814E-02  3.532454E-02  2.422636E-02  2.488419E-02
3.809128E-02  5.465634E-02…
…
```

Figure 6-23. Comparison file pinpower_3D_120_pinonly_P3P3.out excerpt

```
# Time point   1 pin powers (watts) for assembly      1 ring  1 position    1 with total
power  3.794367E+05 watts.
# Number of fuel
pins.....................................................................              19
# Number of duct walls in this
section.....................................................              2
# Number of Z monomials in the explicit
domain.............................................              7
# Number of radial surfaces on the
assembly.....................................................              6
# Number of explicit pin power
meshes.....................................................              35
# Peak of the Peak to Average Pin
Power..................................................... 1.154253832E+00
#Axial  Power Sum (watts/cm)
     1  3.184810E+01
     2  4.882055E+01
     3  7.457178E+01
     4  1.121261E+02
     5  1.656360E+02
…
    33  2.979325E+01
    34  2.294450E+01
    35  2.024073E+01
#Axial Fuel   Monomials (watts/cm)->
#Mesh  PinID         1             2             3             4             5
6             7
     1     1  1.658223E+00  8.674731E-01  2.253283E-01  4.387224E-02  1.172538E-02
2.924283E-03 -7.207973E-03
     1     2  1.657897E+00  8.661425E-01  2.251369E-01  4.635894E-02  1.089878E-02
2.924283E-03 -7.207973E-03
…
     1    18  1.656841E+00  8.632367E-01  2.248883E-01  5.381903E-02  8.418975E-03
2.924283E-03 -7.207973E-03
     1    19  1.657204E+00  8.640243E-01  2.249169E-01  5.133234E-02  9.245576E-03
2.924283E-03 -7.207973E-03
     2     1  2.542631E+00  1.322157E+00  3.369830E-01  6.135727E-02  1.679907E-02 -
1.544843E-04 -2.224312E-03
     2     2  2.542117E+00  1.320080E+00  3.367373E-01  6.522277E-02  1.579989E-02 -
1.544843E-04 -2.224312E-03
…
    35    18  1.064960E+00 -3.903101E-01  3.452252E-02 -3.123007E-02 -4.148675E-03
5.364513E-03  6.518994E-03
    35    19  1.063217E+00 -3.915624E-01  3.512600E-02 -2.947773E-02 -5.733030E-03
5.364513E-03  6.518994E-03
# Time point   1 pin powers (watts) for assembly      2 ring  2 position    1 with total
power  6.621255E+06 watts.
# Number of fuel
pins.....................................................................              271
# Number of duct walls in this
section.....................................................              1
# Number of Z monomials in the explicit
domain.............................................              7
# Number of radial surfaces on the
assembly.....................................................              6
# Number of explicit pin power
meshes.....................................................              35
# Peak of the Peak to Average Pin
Power..................................................... 1.066181478E+00
#Axial  Power Sum (watts/cm)
     1  3.144445E+01
     2  4.821136E+01
…
```

Figure 6-24. Comparison file pinpower_mono_120_pinonly_P3P3.out excerpt

7 Conclusions and Summary

Argonne is supporting the ARDP Natrium Demo project through review of the neutronic methodology developed and applied at TerraPower. To support such review, a neutronic benchmark based on the ABR-1000 core concept was developed.

On the reactivity coefficient analysis completed in Section 4, a detailed description of the methodology, codes and options used at ANL is provided. A variety of specific perturbation options (first order or exact perturbation theory, etc.) are recommended to compute the kinetics parameters (delayed neutron fraction, prompt neutron lifetime), the density coefficients (fuel, coolant, structure), the Doppler effects (flooded and voided), and the axial expansion coefficients (axial, radial and control rod driveline). It should be noted that the analysis summarized here focuses on the neutronic evaluation of these coefficients to support safety analyses done with a code like SAS4A/SASSYS-1. Clear understanding of these modeling approaches are recommended when developing the corresponding SAS model for safety analyses.

On the shutdown margin analysis, the calculation methods and procedures are described in detail and demonstrated using the ABR-1000 benchmark exercise. The shutdown margin analysis assessed the control system worth and the reactivity changes due to the reactor state transitions. Due to the selection of the benchmark problem, the ABR-1000 core at EOEC is not at the most reactive state. Thus, for the actual shutdown margin analysis, additional calculations are needed to evaluate the burnup reactivity swing, the reactivity fault, the overpower fault, and the uncertainties associated with the model and methods.

The pin power reconstruction methodology used in SE2ANL, SE2RCT, and DASSH were discussed in this report. The methodology behind EvaluateFlux was also outlined as it can be used to produce an identical pin power distribution to that used in DASSH. For the pin power comparison, the power in each mesh was imposed to only be produced by the pins. The impact of the angular and spatial approximation in DIF3D-VARIANT was displayed and discussed. For the angular treatment, differences in the pin power distribution for several assemblies was displayed and indicated that diffusion theory produced a result considerably different from the P_3 transport solution while SP_3 was closer. For the spatial flux and source order, using a higher order provided a near negligible difference in the pin power distribution. The reasons for spatial discontinuities in the axial power profiles was explained to come from compositional changes between adjacent meshes, power normalization induced discontinuities, and flux discontinuities. Finally, the files containing axially integrated pin power data and 3D axial pin power evaluations were displayed and explained.

To conclude, this report provides detailed description of the analysis completed at Argonne to compute the reactivity coefficients, shutdown margin and pin power of the ABR-1000, supporting the neutronic methods description performed at TerraPower for licensing the Natrium demonstration reactor.

References

[1] L. Buiron *et al.*, "Benchmarks for Uncertainty Analysis in Modeling (UAM) For Design, Operation and Safety Analysis of SFRs," AEN-WPRS, May 2019.

[2] J. Cahalan *et al.*, "Advanced Burner Reactor 1000MWth Reference Concept," Argonne National Laboratory, ANL-AFCI-202, Sep. 2007. doi: 10.2172/1349893.

[3] N. Stauff, "Status of the NEAMS and ARC neutronic fast reactor tools integration to the NEAMS Workbench: Integration of PyARC/Workbench with New Fast Reactor Modeling and Simulation Capabilities," Argonne National Laboratory, ANL/NEAMS-20/2, Sep. 2020.

[4] P. K. Romano, N. E. Horelik, B. R. Herman, A. G. Nelson, B. Forget, and K. Smith, "OpenMC: A state-of-the-art Monte Carlo code for research and development," *Annals of Nuclear Energy*, vol. 82, pp. 90–97, Aug. 2015, doi: 10.1016/j.anucene.2014.07.048.

[5] C. Lee, Y. S. Jung, and W. S. Yang, "MC^2-3: Multigroup Cross Section Generation Code for Fast Reactor Analysis Nuclear," Argonne National Laboratory, ANL/NE-11-41 Rev.3, Aug. 2018. doi: 10.2172/1483949.

[6] K.L. Derstine, "DIF3D: A Code to solve One-, Two- and Three-Dimensional Finite-Difference Diffusion Theory Problems," Argonne National Laboratory, ANL-82-64, Apr. 1984.

[7] M. A. Smith and C. Lee, "GAMSOR: Gamma Source Preparation and DIF3D Flux Solution," Argonne National Laboratory, ANL/NE-16/50 Rev. 1.0, Jun. 2017.

[8] M. A. Smith and et al., "Perturbation and Sensitivity Tool Based on the VARIANT Option of DIF3D," in *ANS Transaction*, San Diego, Nov. 2012, vol. 107.

[9] M. Atz, M. A. Smith, and F. Heidet, "DASSH software for ducted assembly thermal hydraulics calculations – overview and benchmark," in *Transactions of the American Nuclear Society*, 2020, vol. 123, pp. 1673–1676.

[10] G. Palmiotti, E. E. Lewis, and C. B. Carrico, "VARIANT: VARIational Anisotropic Nodal Transport for Multidimensional Cartesian and Hexagonal Geometry Calculation," Argonne National Laboratory, ANL-95/40, 1995.

[11] M. A. Smith, E. E. Lewis, and E. R. Shemon, "DIF3D-VARIANT 11.0, A Decade of Updates," Argonne National Laboratory, ANL/NE-14/1, 2014.

[12] M. B. Chadwick *et al.*, "ENDF/B-VII.0: Next Generation Evaluated Nuclear Data Library for Nuclear Science and Technology," *Nuclear Data Sheets*, vol. 107, no. 12, pp. 2931–3060, Dec. 2006, doi: 10.1016/j.nds.2006.11.001.

[13] C. Lee and N. Stauff, "Improved Reactivity Worth Estimation of MC^2-3/DIF3D in Fast Reactor Analysis," San Antonio, Texas, 2015.

[14] R. E. Alcouffe, F. W. Brinkley, D. R. Marr, and R. D. O'Dell, "User's Guide for TWODANT: A Code Package for Two-Dimensional, Diffusion-Accelerated, Neutral-Particle Transport," Los Alamos National Laboratory, LA-10049-M, 1990.

[15] G. Rimpault *et al., Current Status and Perspectives of the OECD/NEA sub-group on Uncertainty Analysis in Modelling (UAM) for Design, Operation and Safety Analysis of SFRs (SFR-UAM)*. 2018.

[16] A. E. Waltar, D. R. Todd, and P. V. Tsvetkov, Eds., *Fast Spectrum Reactors*. Boston, MA: Springer US, 2012. doi: 10.1007/978-1-4419-9572-8.

[17] L. Leibowitz and R. A. Blomquist, "Thermal conductivity and thermal expansion of stainless steels D9 and HT9," *Int J Thermophys*, vol. 9, no. 5, pp. 873–883, Sep. 1988, doi: 10.1007/BF00503252.

[18] J. K. Fink and L. Leibowitz, "Thermodynamic and transport properties of sodium liquid and vapor," ANL/RE--95/2, 94649, Jan. 1995. doi: 10.2172/94649.
[19] R. D. Lawrence, "The DIF3D Nodal Neutronics Option for Two- and Three-Dimensional Diffusion Theory Calculations in Hexagonal Geometry," Argonne National Laboratory, ANL-83-1, 1984.
[20] W. S. Yang and M. A. Smith, "Theory Manual for the Fuel Cycle Analysis Code REBUS," Argonne National Laboratory, ANL/NE-19/21, 2020.
[21] K. L. Basehore and N. E. Todreas, "SUPERENERGY-2: a multiassembly, steady-state computer code for LMFBR core thermal-hydraulic analysis," Battelle Pacific Northwest Labs., Richland, WA (USA), PNL-3379; COO-2245-57TR, Aug. 1980. doi: 10.2172/5107861.
[22] W. S. Yang and M. A. Smith, "RCT: REBUS Based Pin Power Reconstruction Using the DIF3D-Nodal and DIF3D-VARIANT Options," Argonne National Laboratory, ANL/NE-14/15, 2014.

Nuclear Science and Engineering Division
Argonne National Laboratory
9700 South Cass Avenue
Lemont, IL 60439-4842

www.anl.gov

Argonne National Laboratory is a U.S. Department of Energy laboratory managed by UChicago Argonne, LLC